LAWRENCE
LIVERMORE
NATIONAL
LABORATORY

Beryllium Dynamic Strength Measurements: Report on Task 1 Agreement #B590737

V. V. Igonin

April 15, 2014

Disclaimer

This document was prepared as an account of work sponsored by an agency of the United States government. Neither the United States government nor Lawrence Livermore National Security, LLC, nor any of their employees makes any warranty, expressed or implied, or assumes any legal liability or responsibility for the accuracy, completeness, or usefulness of any information, apparatus, product, or process disclosed, or represents that its use would not infringe privately owned rights. Reference herein to any specific commercial product, process, or service by trade name, trademark, manufacturer, or otherwise does not necessarily constitute or imply its endorsement, recommendation, or favoring by the United States government or Lawrence Livermore National Security, LLC. The views and opinions of authors expressed herein do not necessarily state or reflect those of the United States government or Lawrence Livermore National Security, LLC, and shall not be used for advertising or product endorsement purposes.

RUSSIAN FEDERAL NUCLEAR CENTER
All-Russia Research Institute of Experimental Physics
VNIIEF

BERYLLIUM DYNAMIC STRENGTH MEASUREMENTS

Report on Task 1
Agreement # B590737
between RFNC – VNIIEF (Russia) and LLNL (USA)

Head of works under Agreement

_____V.V. Igonin

.   . 2011

2011

Contents

Introduction

Goal of the work under Agreement #B590737 is development of experimentally justified model of beryllium shear strength of American production (*Be S200F*) in the pressure range of ~10÷60 GPa and strain rates up to $\dot{\varepsilon}_i \approx 10^6$ s^{-1}.

The *Be* shear strength models, which are available in this range of parameters, have no sufficiently reliable experimental justification.

Therefore it is planned to perform tests using the dynamic method of perturbations [1], [2] with shockless loading of the investigated *Be S200F* samples up to pressure $P_m \approx 55$ GPa. Growth of specified perturbations will be recorded by pulse X-ray radiography. The existing relaxation model of beryllium strength will be corrected basing on test results. Besides, the model should also describe the other published results of tests with investigation of dynamic properties of beryllium.

Also it is planned to perform two tests with loading of beryllium samples up to pressure $P \sim 50 \div 60$ GPa with recovery followed by metallographic investigation. Goal of the metallographic investigation is determination of peculiarities of high-rate deformation of *Be*, determination of density of dislocations and twins in the loaded samples. These data will allow developing a more justified constitutive equation (the strength model).

Objective of this Task of Agreement #B590737 consists of review of the published data on deformation and shear strength of *Be*, as well as numerical-theoretical justification of the tests, which will be performed under the frameworks of Task 3 of the Agreement.

Besides, this report includes the earlier published data on measurements of velocities of vanadium liners accelerated by explosive two-stage device [3], [4].

1 Review of published data on Be strength investigation

1.1 Dynamic deformation

To develop a wide-range model of high-rate deformation, there is need for large scope of experimental data obtained in various areas of stress-strain state (SSS).

For selection of parameters of the model component, which is responsible for strain hardening and influence of strain rate under low pressure, it is common to use the σ-ε diagrams obtained under quasi-static and high-rate loadings, dependences of final length and shape of cylinders on velocity of their impact obtained by the Taylor method, etc. For estimations of thermal softening, there is need for similar data at various temperatures.

1.1.1 σ-ε diagrams of compression-extension at various strain rates and temperatures

Authors of works [5], [6] present results of investigation of beryllium of the types *S200F*, *S200D* and *S200E* (see Fig. 1.1, Fig. 1.2) with grain sizes from 11.4 μm to 27 μm.

Table 1.1 presents composition of beryllium *S200F* with grain size of 15 μm, which was investigated in work [5]. Samples with diameter $\varnothing$=8 mm and length *h*=8 mm were tested [5].

Table 1.1 - Chemical composition of beryllium *S200F* samples [5]

element	*Be*	*BeO*	*Fe*	*C*	*Al*	*Mg*	*Si*	other
%	99.1	0.7	0.08	0.09	0.03	0.01	0.02	<0.04

T=20 ^{o}C

a)

T_0=300 ^{o}C

b)

$\dot{\varepsilon}_i$=2.10^{-2} s^{-1}

c)

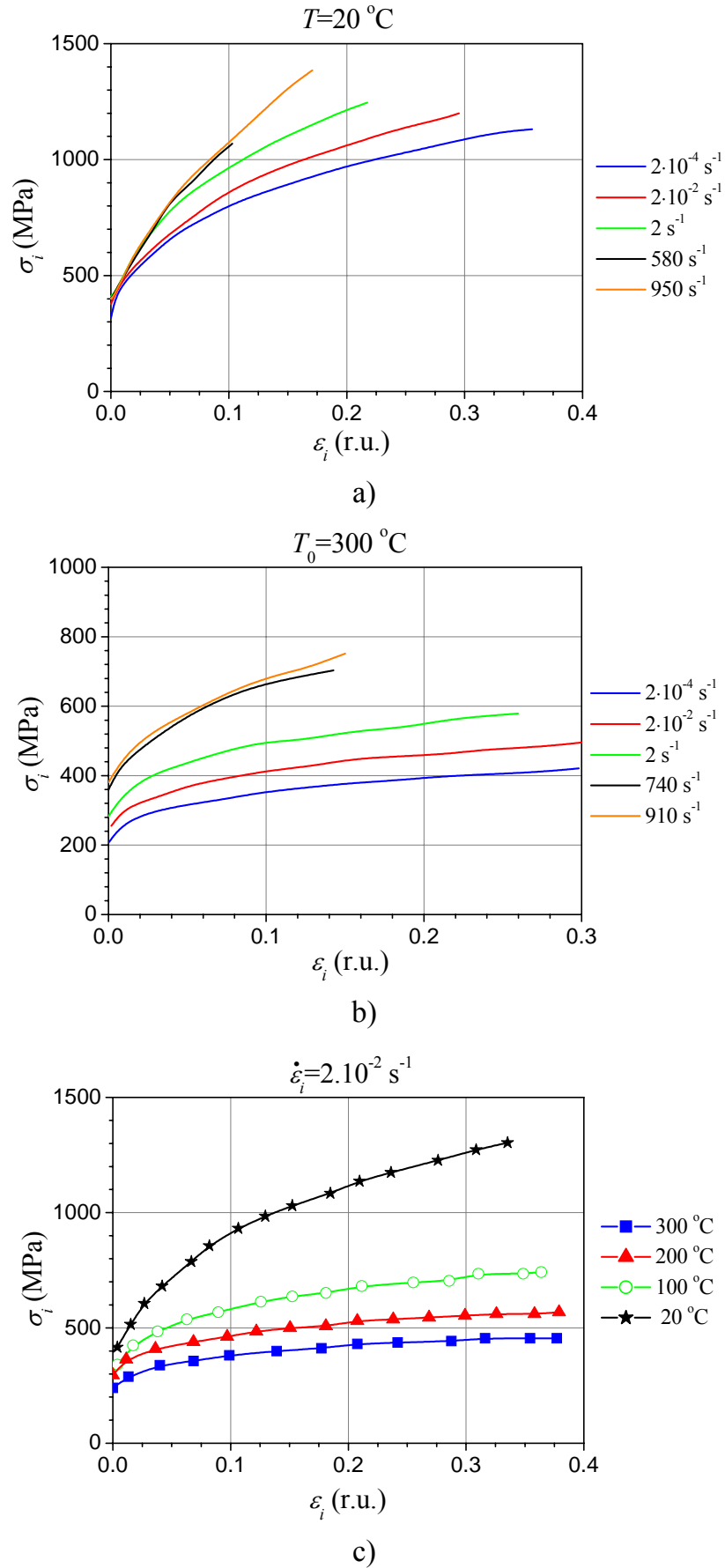Fig. 1.1 - σ-ε diagrams of compression of *S200F* beryllium [5] with grain size of 15 µm
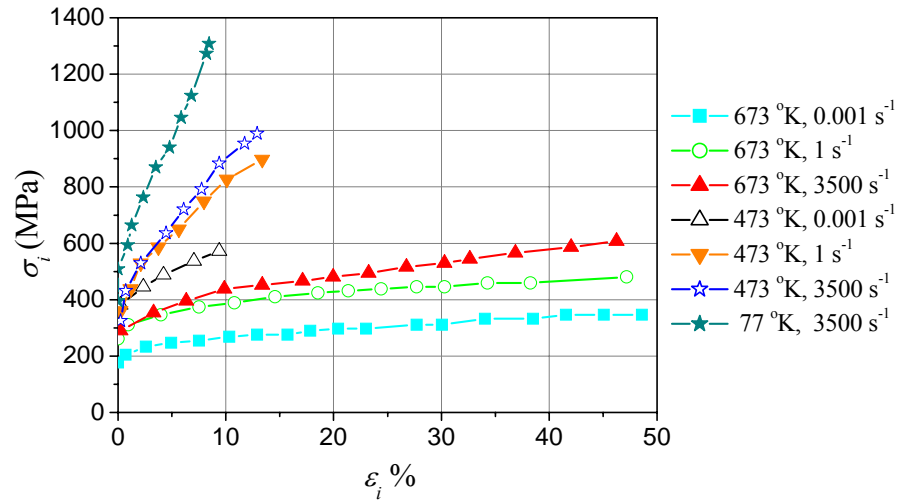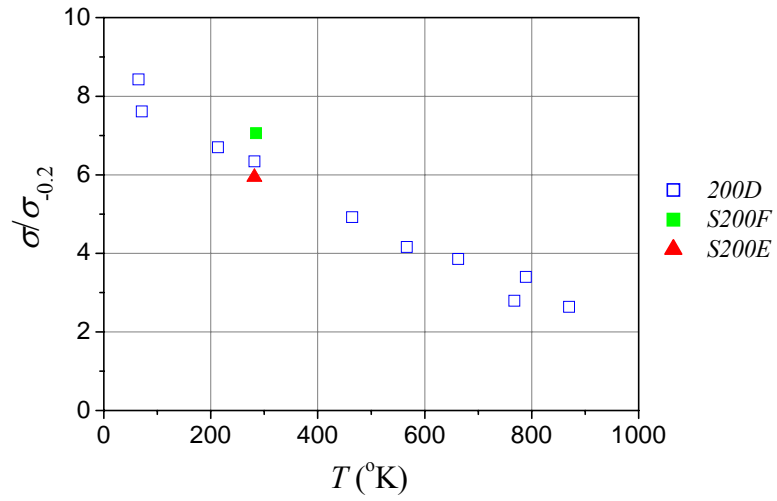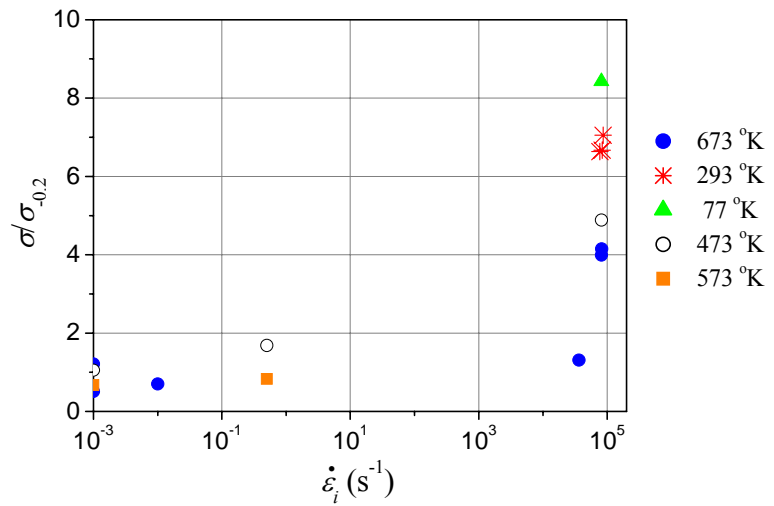
Fig. 1.2 - σ-ε diagrams of compression of *S200F* beryllium [6] with grain size of 11.4 μm

Analysis of the available compression diagrams shows that *S200F* beryllium with grain size of 11.4 μm is rather plastic. It is specially manifested at increased temperatures and strain rates. Authors of work [6] explain this phenomenon by appearance of large number of deformation twins, which were revealed at microstructural analysis of the samples after testing by the SHPB method at normal temperature, strain up to 7 % and strain rate of 1500 s^{-1}. Therefore the significant role of the twinning process in the plastic deformation mechanism at high-rate deformation of *Be* is noted [6]. This mechanism should be taken into account in strength models. All available diagrams point to rather complicated dependence of beryllium behavior on strain rate and temperature.

Fig. 1.3 [7] presents the available data, which were obtained by the SHPB method for compression at strain rate of 1550 s^{-1}. The diagram was obtained up to deformation of ~8 %.
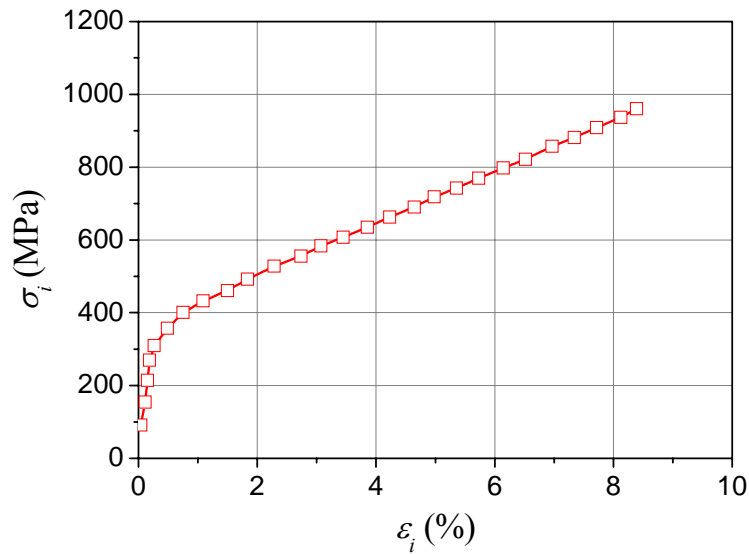

Fig. 1.3 - σ-ε diagrams of beryllium compression at $\dot{\varepsilon}_i$ =1550 s^{-1} [7]

1.1.2 Taylor method

Influence of strain and its rate can be estimated basing on simulation of dynamic deformation of uniaxial compression of cylinders at strain rate $\dot{\varepsilon}_i^p = 10^5$ s^{-1} (the Taylor method). Authors of work [8] performed investigations of beryllium samples with initial density ρ_0=1.84 g/cm^3 and length L_0=2.347 cm. Results of measurement of the rate and the relative change of the final length of the cylinders are presented in Table 1.2.

Table 1.2 – Results of tests with *S-200* beryllium by Taylor method

W (m/s)	158	181	203	205	273
(L_f/L_0) exp	0.970	0.963	0.958	0.953	0.932

For *S200F* beryllium, authors of work [5] obtained profiles of cylinders after impact of them against a rigid barrier with velocity W=216 m/s at normal temperature T=20 °C and increased temperature T=300 °C. The initial cylinder sizes were the following: diameter $\varnothing$=8 mm and length h=20 mm. Fig. 1.4 shows the final digitized profiles of cylinders (length L and radius R).
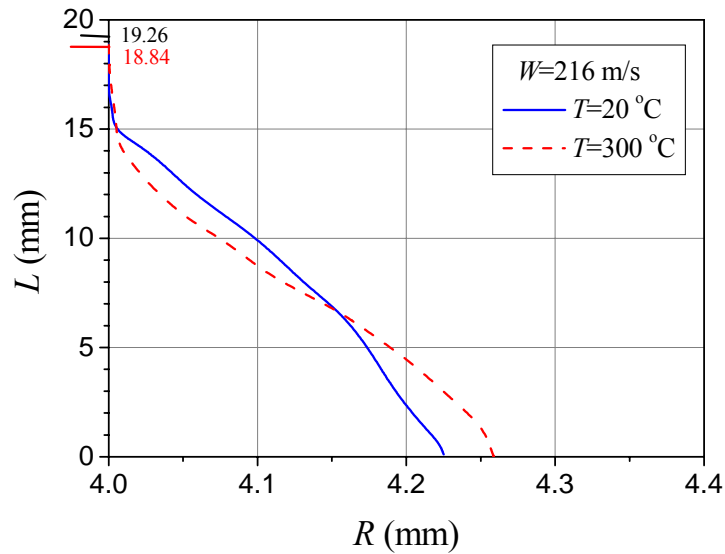
Fig. 1.4 – Experimental profiles of cylinders, which were obtained in test by Taylor method at impact velocity W=216 m/s and T=20 and T=300 °C

1.2 Shock-wave loading

1.2.1 Measurement of profiles of free surface velocity

For *S200F* beryllium, authors of work [5] measured profiles of free surface velocity of shock-wave loaded samples (pressures *P*=0.97 GPa; 1.63 GPa, 3.73 GPa, 6.12 GPa). The initial sizes of the samples were the following: diameter ∅=30 mm and height *h*=4 mm. Fig. 1.5 shows dependences of free surface velocity on time of shock-loaded *S200F* beryllium samples.
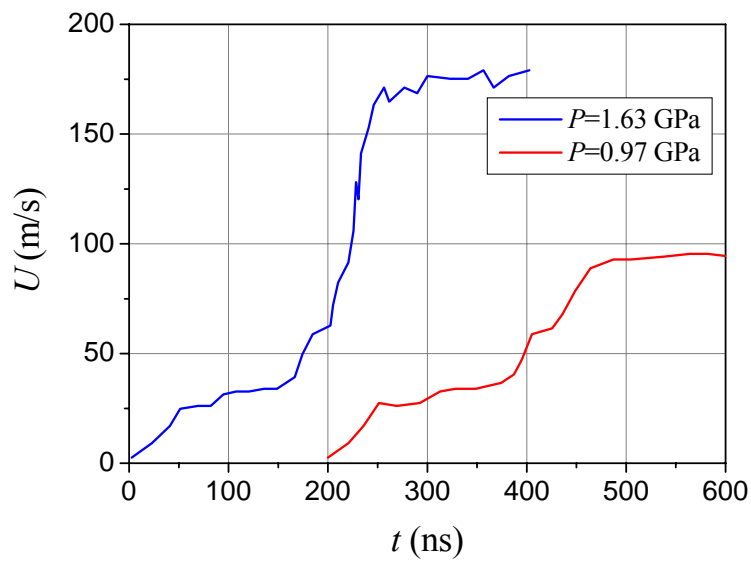
a)
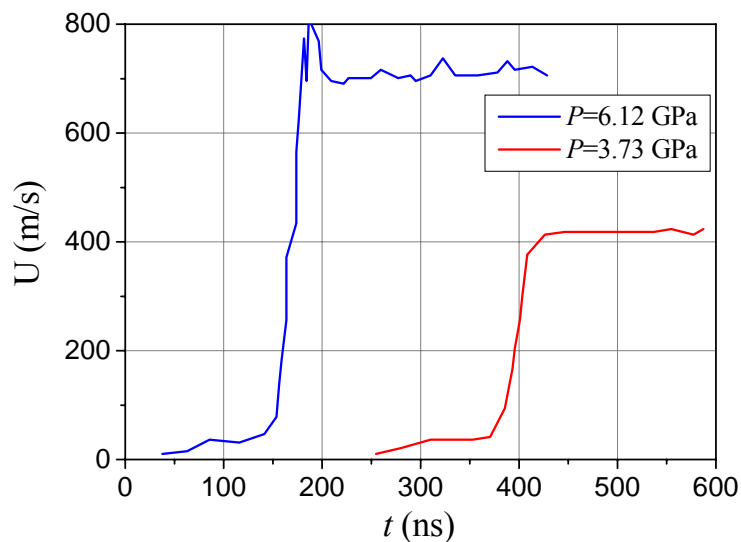
b)

Fig. 1.5 – Profiles of *S200F* beryllium free surface velocity, which were obtained at normal temperature in work [5]

In work [9], *S200F* beryllium with the following parameters was investigated: sound velocities C_L=13.19-13.20 mm/μs, C_S=9.04-9.07 mm/μs, density of 1.85 g/cm^3, grain size of 11.4 μm. Fig. 1.6 shows a scheme of the experimental setup.

Fig. 1.6 – Scheme of experimental setup

Fig. 1.7-Fig. 1.9 and Table 1.3 present results of tests in various scales.

Fig. 1.7 – Free surface velocity versus time

Fig. 1.8 – Free surface velocity versus time

Fig. 1.9 – Free surface velocity versus time

Table 1.3

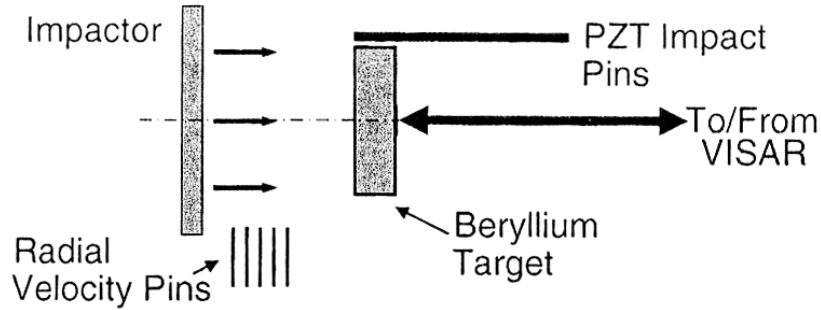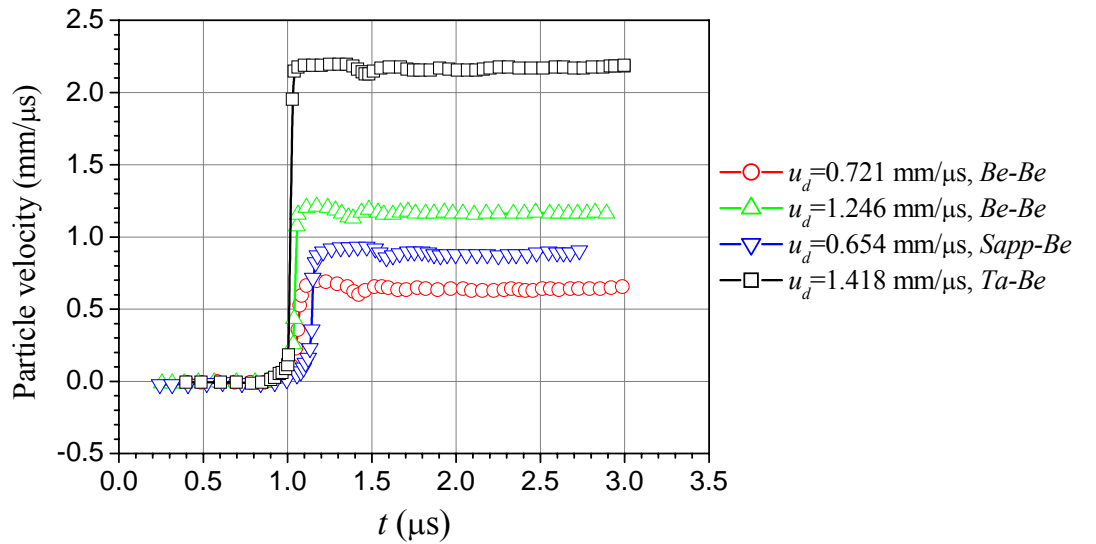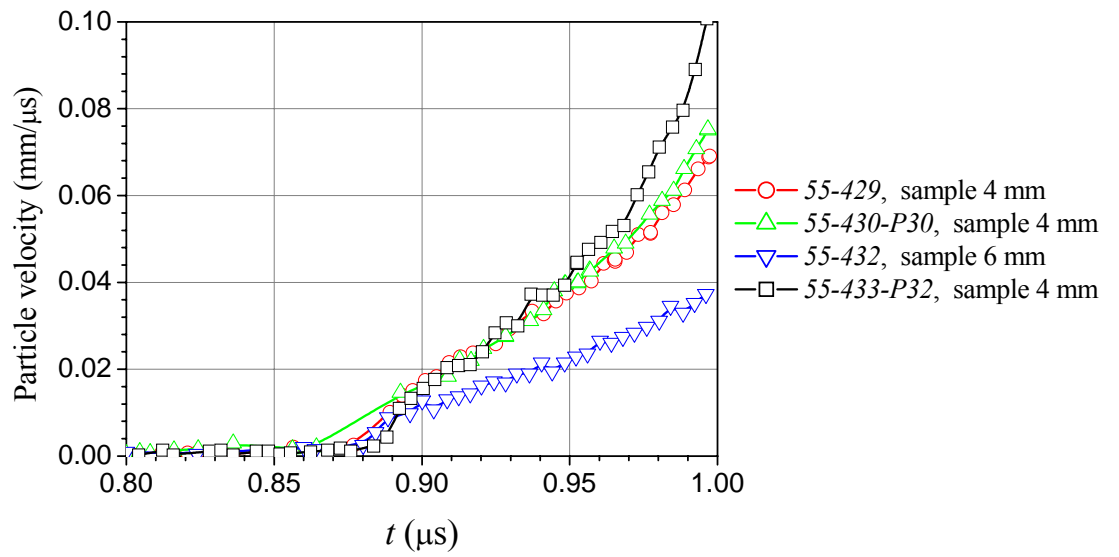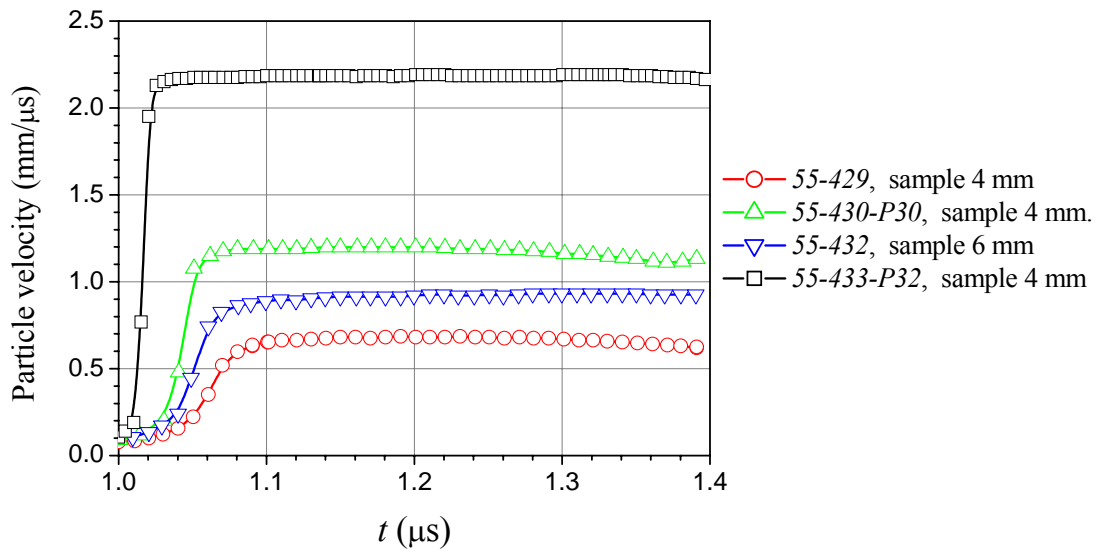| Test	Impactor/ target	Impactor velocity (mm/μs)	Target thickness (mm)	Hugoniot limit (GPa)	Stress (GPa)	$\sigma^1_{spall}/\sigma^2_{spall}$ * Spall strength (GPa)
55-429	*Be/Be*	0.721	3.9850	0.150	5.56	0.609/0.857
55-430-P30	*Be/Be*	1.246	3.9665	0.166	10.20	0.638/0.898
55-432	*Sapphire/Be*	0.654	5.9630	0.104	7.66	0.572/0.810
55-433-P32	*Ta/Be*	1.418	3.9875	0.169	19.25	0.525/0.842

*Value of spall strength σ^1_{spall} was calculated by the formula $\sigma^1_{spall} = \rho_0 \cdot C_0 \cdot \dfrac{\Delta W}{2}$, the value σ^2_{spall} was obtained by the Romanchenko-Stepanov relation [10].

In works [11], [12], planar samples of beryllium were subjected to effect of impactors accelerated in powder gun. The sample surface, which is opposite to the impactor, is covered by a screen made of *LiF* monocrystal, which is oriented in the direction <100>. Data on the experimental setup are presented in Table 1.4.

Table 1.4 - Data on experimental setup [11]

Number of test	Impactor material	Velocity of impactor approach (km/s)	Sample thickness
Be18	*Z*-section of sapphire	0.536	8.049
Be3	*Z*-section of sapphire	0.871	3.946
Be8	*Z*-section of sapphire	0.899	8.062
Be19	*Z*-section of sapphire	0.946	8.062
Be9	beryllium	1.984	8.063
Be4	beryllium	2.040	3.896
Be14	aluminum	1.969	9.019
Be15	copper	1.987	9.027
Be2	copper	1.990	3.947

The experimental results are shown in Fig. 1.10 [12].
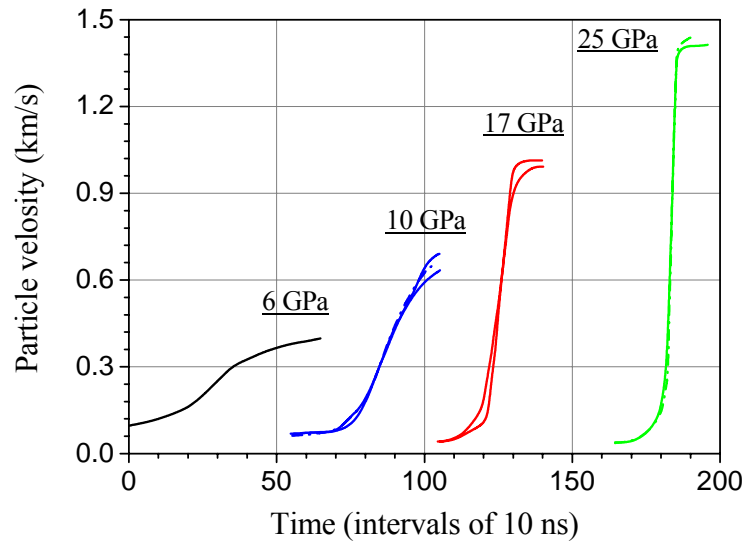
Fig. 1.10 – Typical wave profiles at external boundary of sample

Beryllium was investigated in work [13]. Its basic characteristics and the loading conditions are presented in Table 1.5 and Table 1.6.

Table 1.5 – Basic characteristics

Density	ρ=1.85 g/cm^3
Longitudinal sound velocity	C_l=12.55 km/s
Young's modulus	E=300 GPa
Shear modulus	G=145 GPa
Velocity of transverse sound waves	C_n=8.83 km/s
Poisson's ratio	v=0.03

Table 1.6 – Первичные результаты экспериментов

N. of imp.	H_m (mm)	h_{imp} (mm)	U'_{imp} (m/s)	U_{imp} (m/s)	U_{fs}^{max} (m/s)	δv (m/s)	Δv_{max} (m/s)	W (m/s)	Δt (ns)	Note
301	6.88	1.99	19.4	16.8	16.8	0	0	-	0	impactor *St3*
304	6.92	1.94	64	56	56	0	0	-	520	impactor *D16*
303	6.92	1.92	99	85.6	87.4	-1.8	0	74.9	600	impactor *D16*
300	6.92	2.01	138	120	121.1	-1.1	0	86.8	360	impactor *D16*
307	4.98	1.88	139	120.9	127.7	-6.9	0	90	315	impactor *D16*
308	3.96	1.88	142.7	123.9	135.3	11.4	0	-	238	impactor *D16*
306	5.98	1.88	143	124.2	125	-0.8	0	84.4	385	impactor *D16*
309	2.97	1.87	147.3	127.9	141.7	13.8	7.6	-	160	impactor *D16*
297	6.92	2.01	100	133.5	130.2	3.3	5.5	-	765	impactor *St3*
302	6.92	1.92	205	177.6	178.8	-1.2	0	101.5	355	impactor *D16*
298	6.90	2.01	159	212.4	208.2	4.2	0	-	535	impactor *St3*
305	6.93	1.89	249	216.3	219.8	-3.5	7.9	101.7	325	impactor *D16*
299	6.91	1.98	198	265.3	264.2	-1.1	7.6	92.4	405	impactor *St3*
256	6.95	1.47	213	285	276.6	8.4	19.4	111.1	415	impactor *St3*

In Table 1.6, h_t h_{imp} are thicknesses of target and impactor, respectively; U'_{imp}, U_{imp} are impactor velocity in particular test and that recalculated for the case of symmetric impact when materials of the impactor and the target are similarж U_{fs}^{max} is the maximum value of free surface velocity; δv is difference between impactor velocity and maximum velocity; Δv_{max} is the value of width of distribution in velocities or diffusion velocity (square root from dispersion of average velocity); W is the value of spall velocity («pullback»); Δt is the time interval between elastic precursor and spall.

The values of normal stress and strain were calculated with use of the following formulas:

$$\sigma = 0.5\rho[U_{max}C_P + U_{HEL}(C_{HEL} - C_P)],$$
$$\varepsilon = 0.5 \cdot [U_{max}/C_P + (U_{max} - U_{HEL})/C_P],$$

where C_P is velocity of plastic front of compression wave.

Calculated values of the dynamic variables, which were obtained basing on data from Table 1.6 and the formulas, are presented in Table 1.7.

Table 1.7 – Calculated values of dynamic variables

N. of imp.	h_{tg} (mm)	U_0 (m/s)	U_{max} (m/s)	C_p (km/s)	U_{HEL} (m/s)	σ_{HEL} (GPa)	ε_{HEL} (10^{-3})	σ_{pl} (GPa)	ε_{pl} (10^{-2})
9	6.92	56	56	8.71	22.0	0.255	0.876	0.529	0.283
8	6.92	85.6	87.4	8.63	24.5	0.284	0.976	0.786	0.462
5	6.92	120	121.1	8.53	22.7	0.263	0.904	1.039	0.667
2	6.92	133.5	130.2	8.48	24.4	0.283	0.972	1.112	0.721
7	6.92	177.6	178.8	8.32	22.1	0.256	0.880	1.461	1.030
3	6.90	212.4	208.2	8.20	22.4	0.260	0.892	1.668	1.222
10	6.93	216.3	219.8	8.13	22.2	0.257	0.884	1.742	1.304
4	6.91	265.3	264.2	7.93	22.4	0.260	0.892	2.032	1.614

The second series of tests on dynamic loading was performed with samples of different thicknesses. Results of tests of samples from this series are presented in Table 1.8. Designations from Table 1.8 are similar to designations from Table 1.6.

Table 1.8

N	h_t mm	U_{imp}, m/s	U_{max}, m/s	δU m/s	U_{hole}, m/s	U_{hole}/U_{max}	U_{HEL}, m/s	C_P, km/s
14	2.97	127.9	141.7	-13.8	119	0.84	32.9	8.34
13	3.96	123.9	135.3	-11.4	117.5	0.868	29.8	8.51
12	4.98	120	127.8	-6.9	114	0.892	26.6	8.52
11	5.98	124.2	125	-0.8	112.5	0.9	24.2	8.48
5	6.92	120	121.1	-1.1	113	0.933	22.7	8.53

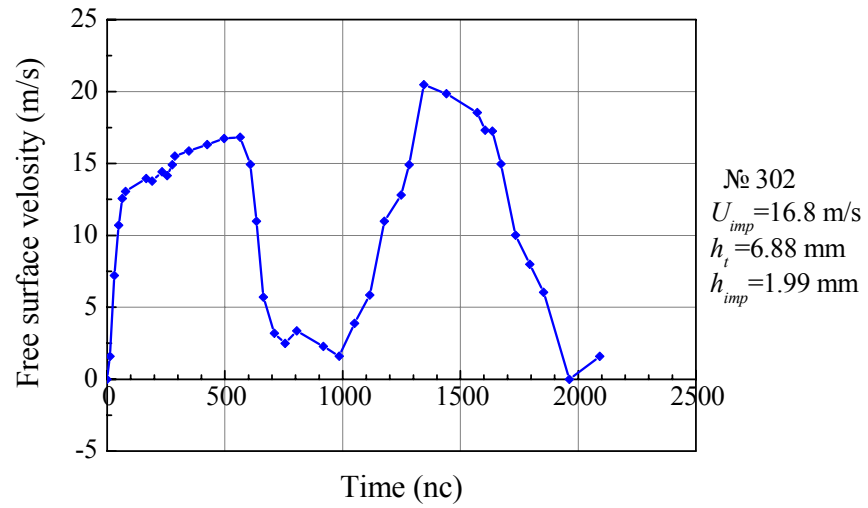Results of measurements of beryllium free surface velocity are shown in Fig. 1.11-Fig. 1.24.
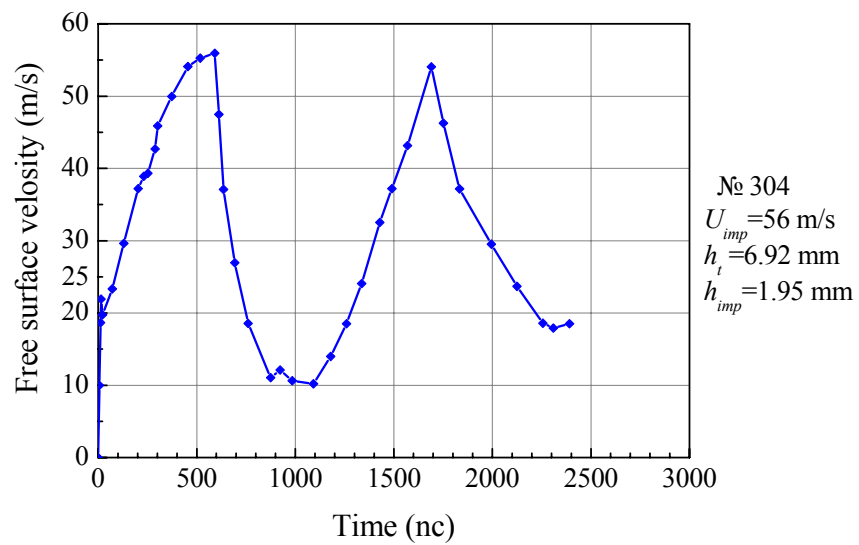
№ 302
U_{imp} =16.8 m/s
h_t =6.88 mm
h_{imp} =1.99 mm

Fig. 1.11 – Profile of beryllium free surface velocity

№ 304
U_{imp} =56 m/s
h_t =6.92 mm
h_{imp} =1.95 mm

Fig. 1.12 – Profile of beryllium free surface velocity

№ 303
U_{imp}=85.6 m/s
h_t=6.92 mm
h_{imp}=1.92 mm

Fig. 1.13 – Profile of beryllium free surface velocity

№ 300
U_{imp}=120 m/s
h_t=6.92 mm
h_{imp}=2.01 mm

Fig. 1.14 – Profile of beryllium free surface velocity

№ 307
U_{imp}=120.9 m/s
h_t=4.98 mm
h_{imp}=1.88 mm
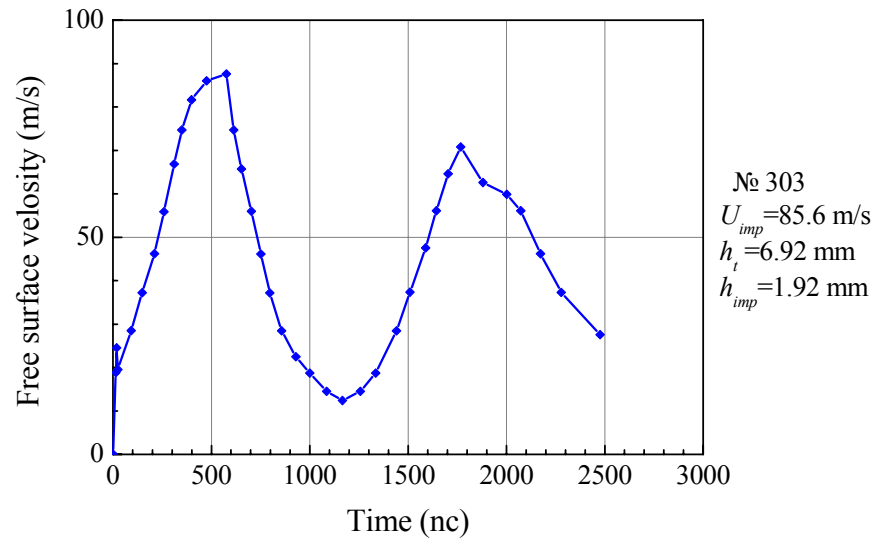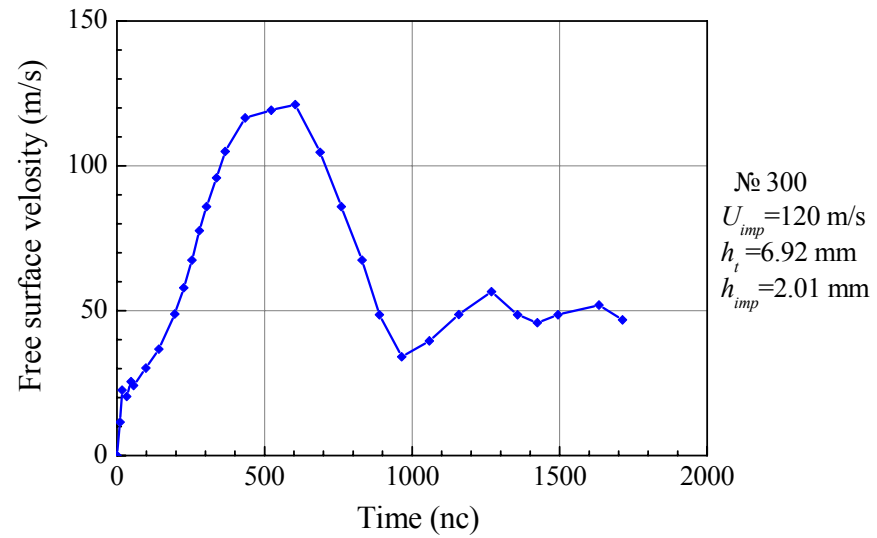
Fig. 1.15 – Profile of beryllium free surface velocity

№ 308
U_{imp}=123.9 m/s
h_t=3.96 mm
h_{imp}=1.88 mm

Fig. 1.16 – Profile of beryllium free surface velocity

№ 306
U_{imp}=124.2 m/s
h_t=5.98 mm
h_{imp}=1.88 mm

Fig. 1.17 – Profile of beryllium free surface velocity

№ 309
U_{imp}=127.9 m/s
h_t=2.97 mm
h_{imp}=1.87 mm

Fig. 1.18 – Profile of beryllium free surface velocity

№ 297
U_{imp} =133.5 m/s
h_t =6.92 mm
h_{imp} =2.01 mm

Fig. 1.19 – Profile of beryllium free surface velocity

№ 302
U_{imp} =178.8 m/s
h_t =6.92 mm
h_{imp} =1.96 mm

Fig. 1.20 – Profile of beryllium free surface velocity
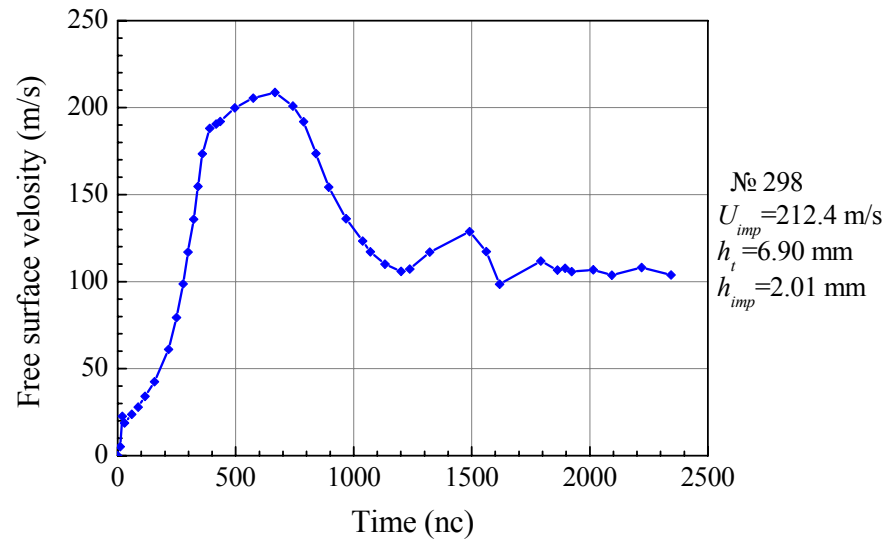
Fig. 1.21 – Profile of beryllium free surface velocity

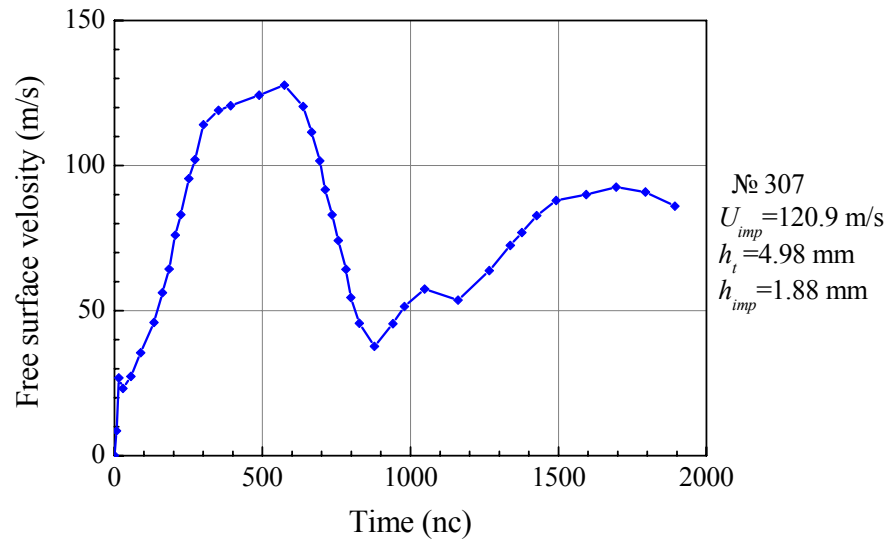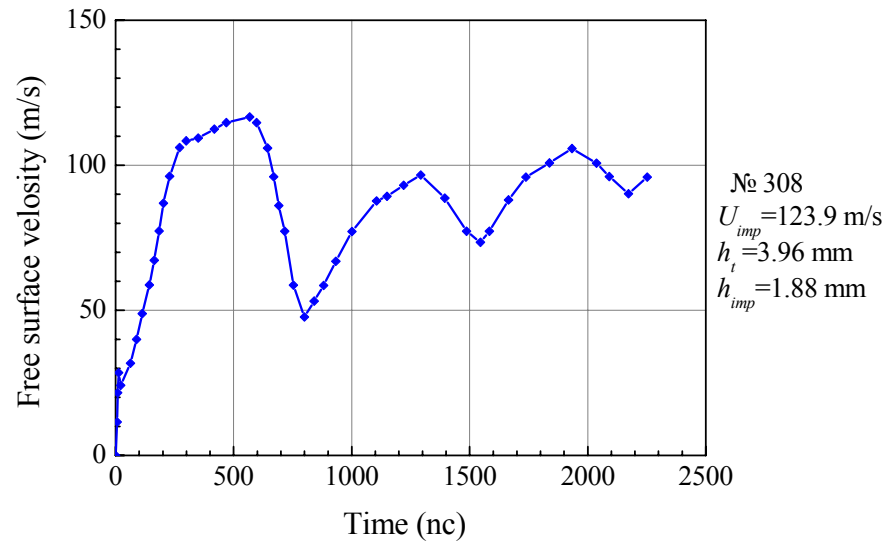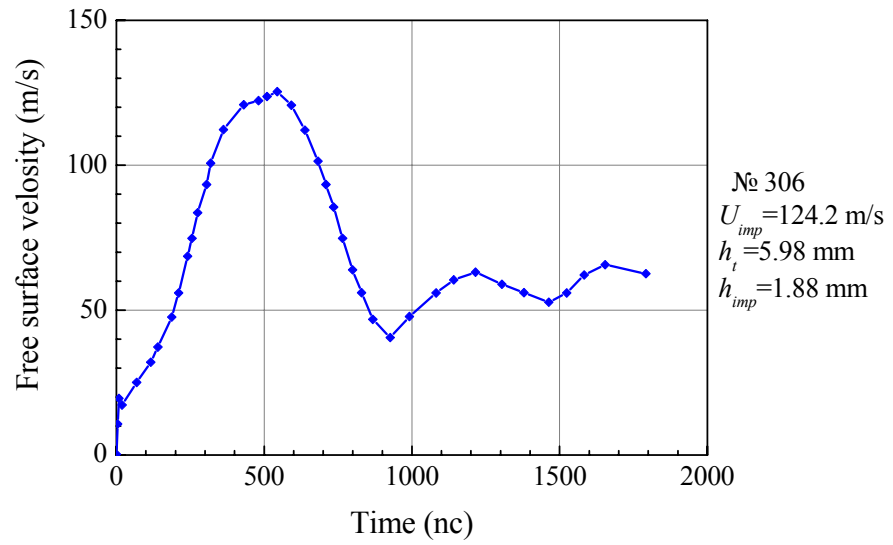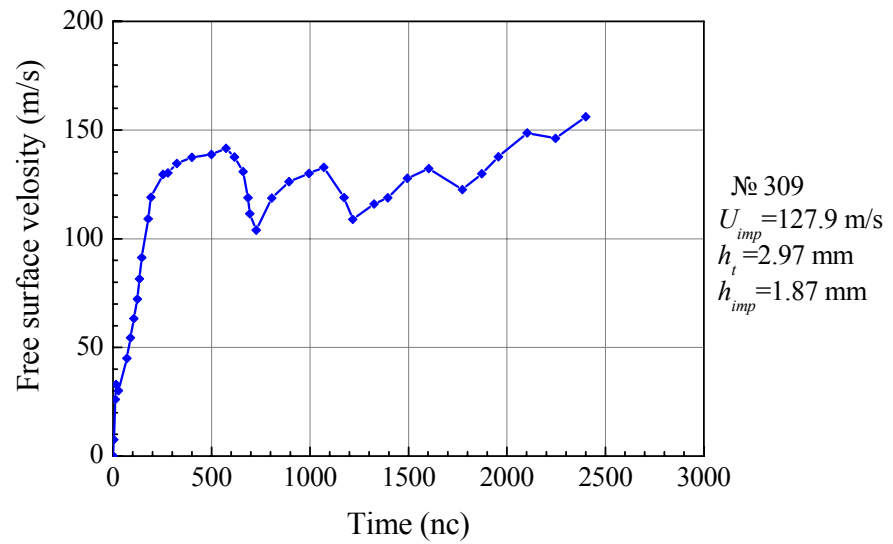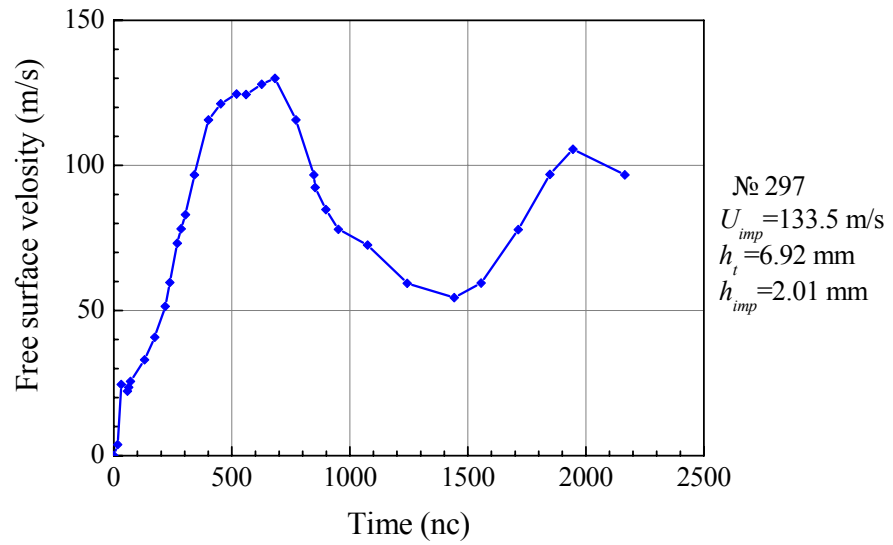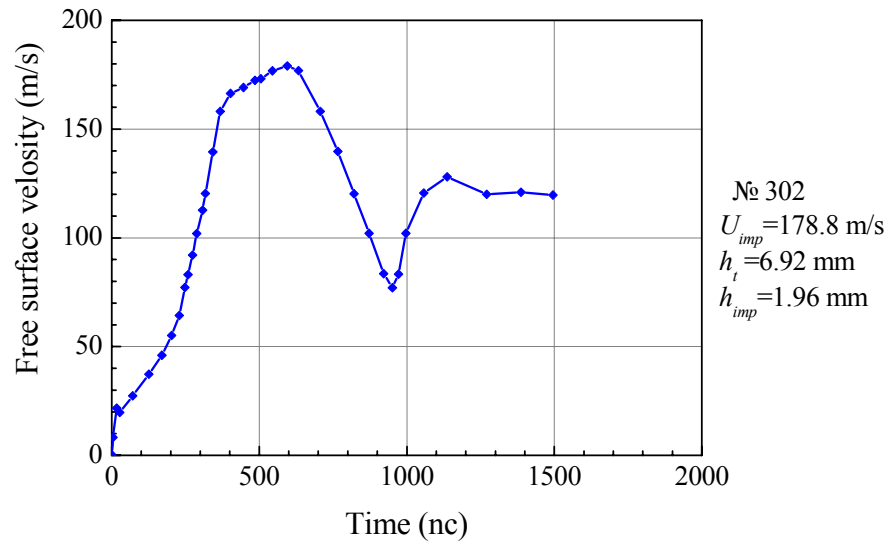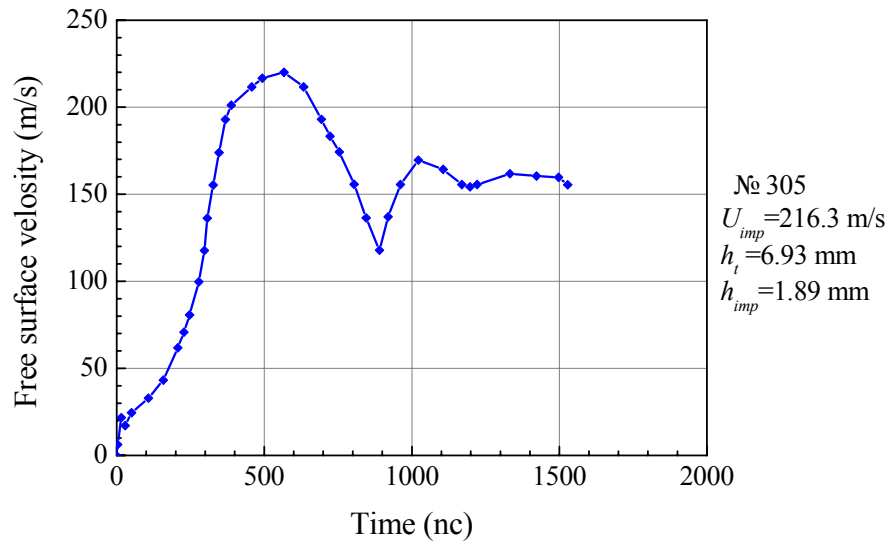Fig. 1.22 – Profile of beryllium free surface velocity
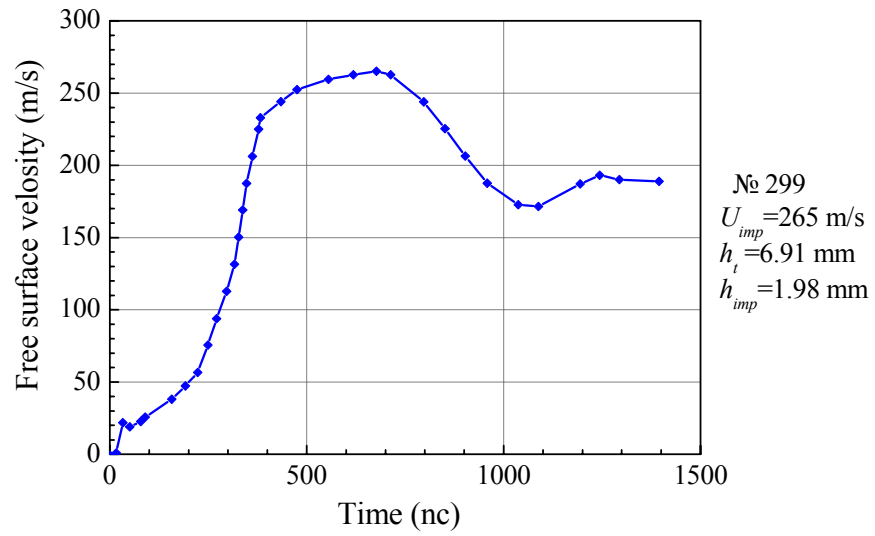
Fig. 1.23 – Profile of beryllium free surface velocity
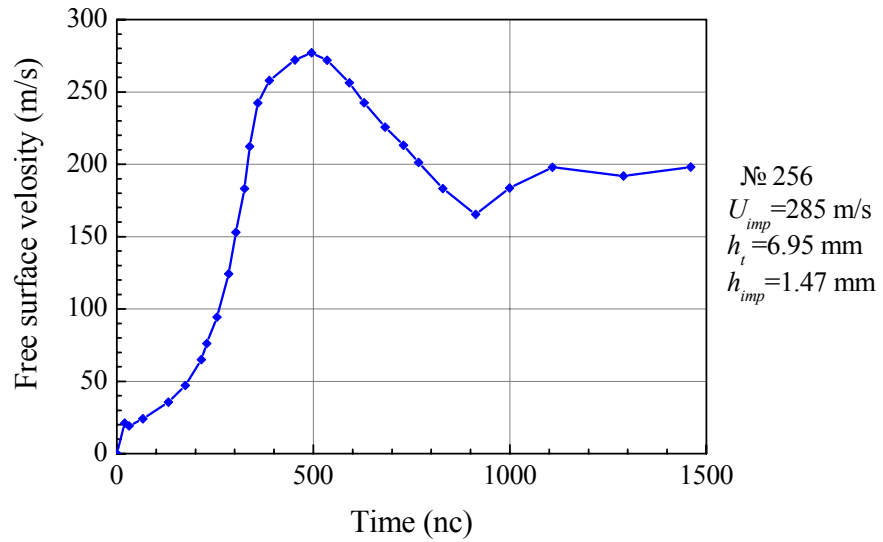
Fig. 1.24 – Profile of beryllium free surface velocity

1.2.2 Measurement of shock wave front width

Experimental data for beryllium were obtained by Swegle and Gready with use of interferometer [14]. Fig. 1.25 and Fig. 1.26 show profiles of free surface velocity and results of measurement of strain rate dependence on amplitude of shock compression pressure.
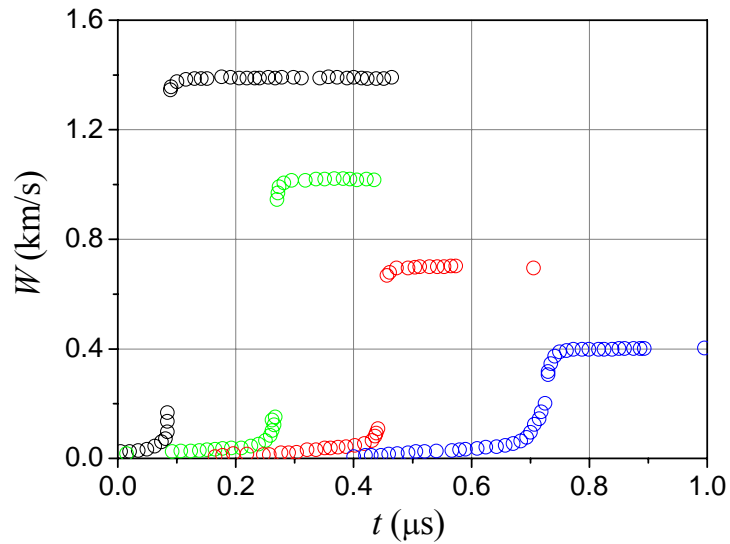
$\bigcirc$ - σ_X=6.5 GPa, $\bigcirc$ - σ_X=11.5 GPa, $\bigcirc$ - σ_X=17.4 GPa, $\bigcirc$ - σ_X=24.5 GPa

Fig. 1.25 - Experimental dependences of free surface velocity
on time for *Be* [14]
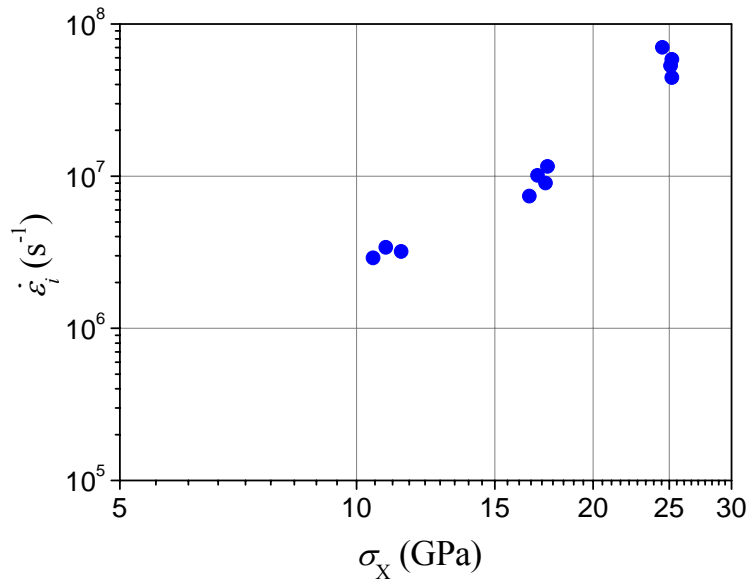
Fig. 1.26 - Strain rate versus shock wave amplitude

1.2.3 Measurement of sound velocities

Fig. 1.27 shows experimental values of elastic and volume sound velocity of beryllium [15] [16].

■, ▽ – test [15];
△, ○ – test [16].

Fig. 1.27 – Experimental dependences of elastic and volume sound velocity of beryllium on value of main normal stress

1.2.4 Method of main stresses

The method of main stresses was used to perform a series of tests aimed to investigate shear strength of beryllium. The experimental results are presented in work [7]. In the tests with measurement of shear strength of materials by the method of main stresses, gauges of small thicknesses made of manganin wire PEMS with diameter of 0.05 mm, which are covered by insulating materials (lavsan band of the type *LT-19* 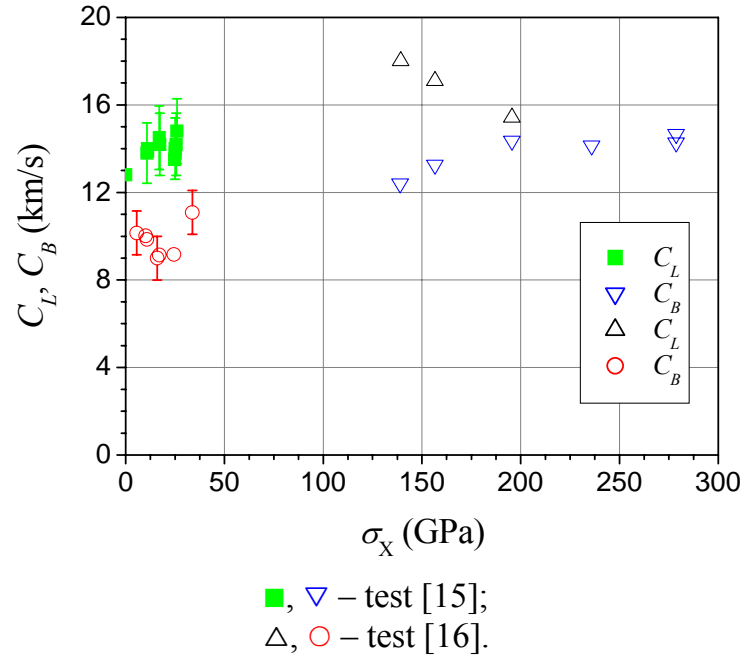with the thickness of 0.04 mm, the total thickness of the gauges with additional fluoroplastic insulation was varied within 0.23-0.53 mm), are placed in cuts (Δ=0.23÷0.53 mm), which are prepared in the sample of the investigated material parallel and perpendicularly to the front of the propagating shock wave. Fig. 1.28 presents the basic scheme of the tests. The investigated beryllium had the following percentages: 98.65, 98.98 and 99.06 % and the densities ρ_0=1.851, 1.851 and 1.854 g/cm^3, respectively.

The planar compound samples had the diameter of 60 mm and the thickness of 20 mm. Geometric sizes of the sample are shown in Fig. 1.29. Planar shock waves of various intensities were generated in the investigated sample by explosive contact devices with the known parameters of SW in screens made of copper and aluminum.
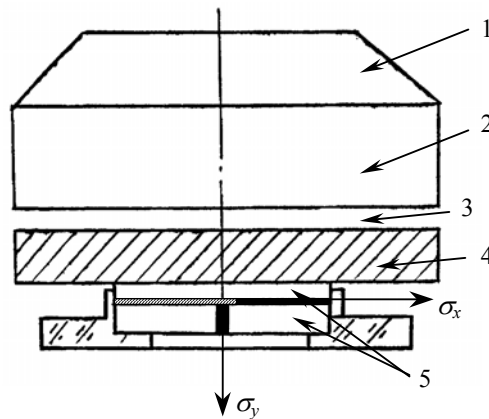
1 – lens;
2 – HE cartridge;
3 – air gap;
4 – copper cover;
5 – sample elements.

Fig. 1.28 – Scheme of experimental assembly
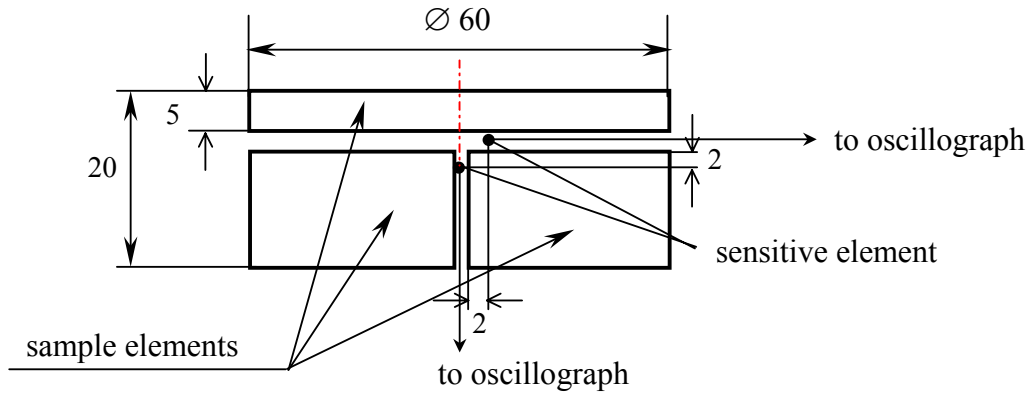
Fig. 1.29 - View of investigated beryllium sample

The experimental results are presented in Table 1.9

Table 1.9

% of beryllium	σ_X (GPa)	σ_y (GPa)
	2.5	2.3
	3.0	2.8
	3.0	2.6
98.65	12.5	11.5
	13.0	12.0
	18.5	17.0
98.98	3.7	3.5
	13.6	12.6
	3.1	3.0
	3.0	2.9
	7.6	7.0
	7.3	6.8
99.06	12.8	12.2
	13.4	12.4
	17.6	16.0
	19.7	18.2

1.2.5 Method of perturbation growth recording

The other method for investigation of metal shear strength is the method of perturbation growth recording [17]. Schemes of one-stage and two-stage assemblies are presented in Fig. 1.30. The gap between the HE surface and the investigated liner provides quasi-isentropic loading regime.

One-stage assembly

Two-stage assembly

1 - generator of planar detonation wave;
2 - HE: $\varnothing 120 \times 60$ mm;
3 - vacuumized gap: $\delta = 2$ mm;
4 - studied liner: *Be*, $\varnothing 80 \times 2$ mm;
5 - sealing cylinder.

1 - generator of planar shock wave;
2 - HE of first stage: $\varnothing 120 \times 90$ mm;
3 - damper: plexiglass, $\varnothing 120 \times 2$ mm;
4 - impactor: *Fe*, $\varnothing 120 \times 2.2$ mm;
5 - vacuumized gap: $\delta = 20$ mm;
6 - HE of second stage: $\varnothing 120 \times 10$ mm;
7 - vacuumized gap: $\delta = 2$ mm;
8 - studied liner: *Be*, $\varnothing 50 \times 2$ mm;
9 - sealing cylinder.

Fig. 1.30 - One-stage and two-stage assemblies

Perturbation wavelength was 2 mm, perturbation amplitude was varied.

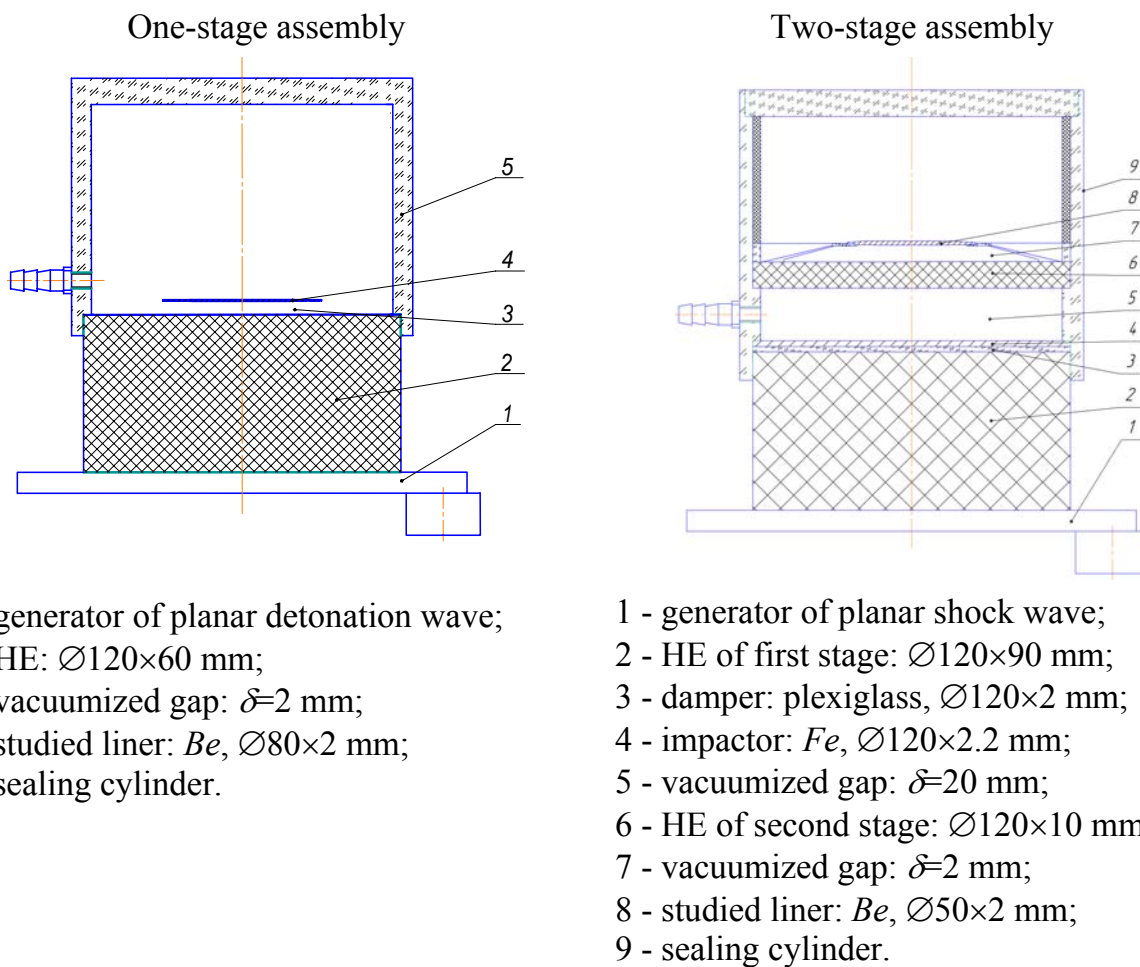Facility «Eridan-3» was the source of *X*-ray radiation. Its boundary radiation energy was 1 MeV; pulse duration at half-height was ~0.1 µs.

Information on growth of periodic perturbations was obtained using X-ray images of free surface of the studied sample. In the tests, X-ray image was recorded by the recording system basing on ten ADC-CR screens. The typical X-ray images of the liners in flight are shown in Fig. 1.31.
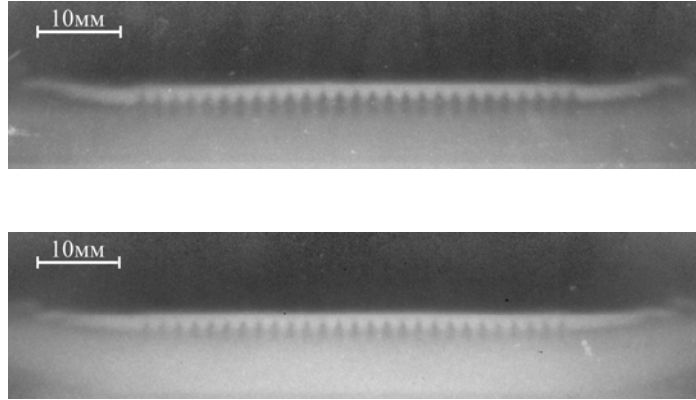
Fig. 1.31 - Explosive X-ray photos of investigated liner

Fig. 1.32 presents experimental results on recording of perturbation growth in beryllium liners under quasi-isentropic loading up to pressures $P{\approx}30$ GPa and $P{\approx}50$ GPa.

a) $P{\approx}30$ GPa
b) $P{\approx}50$ GPa
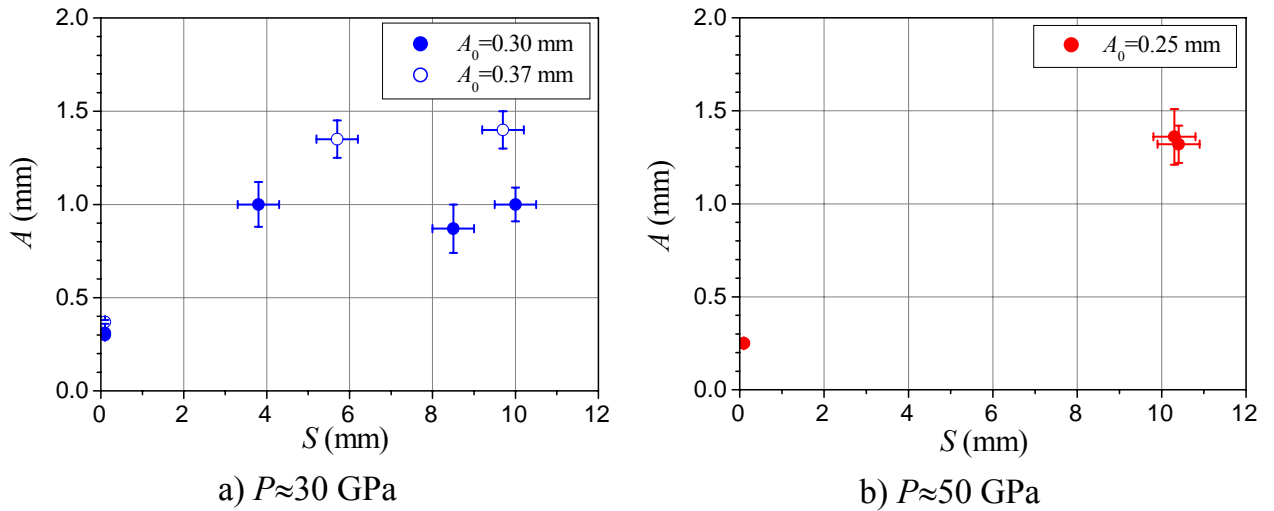
Fig. 1.32 – Results of measurement of perturbation amplitude growth on beryllium surface

The following designations are used in Fig. 1.32: A is the range of perturbation amplitude, $A=2a_0$, where a_0 is a usual designation for amplitude of periodic perturbations.

2 Models of Be strength

2.1 Steinberg model

For *S-200* beryllium in work [18], the Steinberg model is presented as a function of intensity of plastic strains ε_i^p, pressure *P*, increment of temperature ΔT and relative compression δ:

$$Y_S = Y_0 f_1(\varepsilon_i^p) \cdot [1 + f_2(P, \delta) + f_3(\Delta T)], \tag{2.1}$$

where f_1 takes account for deformation hardening, and it has limitation in its value Y_0:$f_1(\varepsilon_i^p) \leq Y_{max}$, $Y_0 = \dfrac{1 - 2\nu}{1 - \nu} \sigma_{HE}$, and the Y_{max} value corresponds to maximum, which is experimentally revealed in the tests with intensive plastic strain. Analytical relations for separate functions have the following forms in equation (1.2):

$$f_1(\varepsilon_i^p) = \left[1 + \beta(\varepsilon_p - \varepsilon_{p0})\right]^n, \quad f_2(P) = \left(\frac{\partial Y}{\partial P}\right)_T \frac{P}{Y_0 \delta^{\frac{1}{3}}},$$

$$f_3(\Delta T) = \left(\frac{\partial Y}{\partial T}\right)_p \frac{\Delta T}{Y_0} \tag{2.2}$$

where β, *n* are the hardening parameters; δ is the substance compression.

In work [18], the dependence of shear modulus *G* on pressure *P* and *T* is specified by the relation:

$$G = G_0 \left[1 + \left(\frac{\partial G}{\partial P}\right)_T \frac{P}{G_0 \delta^{\frac{1}{3}}} + \left(\frac{\partial G}{\partial T}\right)_p \frac{\Delta T}{G_0}\right], \tag{2.3}$$

where G_0 is the shear modulus in normal state.

The following values of the parameters are selected for beryllium: G_0=151GPa, Y_0=0.33GPa, Y_{max}=1.23GPa, β=81, *n*=0.22, $\dfrac{\partial G_P}{\partial G_0}$=15.5, $-\dfrac{\partial G_T}{\partial G_0}$=0.26, T_{m0}=1820, γ_0=1.11, *a*=1.0 [18].

2.2 *Johnson-Cook model*

In the area of dynamic deformation ($\varepsilon_i^P < 0.2$, $\dot{\varepsilon}_i < 10^3 s^{-1}$, 297 °K$\leq T \leq$573 °K, $P<$1 GPa), the equation, which is close to the Johnson-Cook model [19] in form, is used:

$$Y_S = Y_0 \cdot \left[1 + \frac{a_0}{T} \cdot \left(\varepsilon_i^p\right)^n\right] \cdot \left[1 + \frac{b_0}{\left(1 - \frac{T}{T_{0m}}\right)^k} \cdot \left(\ln\frac{\dot{\varepsilon}_i}{\dot{\varepsilon}_{io}}\right)^m\right] \cdot \left[1 - c\frac{T}{T_{0m}}\right], \tag{2.4}$$

where Y_0=0.35 GPa, a_0=1250 1/degree, n=0.35, b_0=0.018, m=0.97, k=3.4, c=1.04 are constant coefficients, which are selected basing on the experimental σ-ε diagrams of *Be* compression at various strain rates and temperatures, which were published in work [5]. It is noted that the dependence of yield strength on temperature is complicated.

2.3 *Phenomenological functional model of strength (PMS) (VNIIEF)*

Development of beryllium shear strength model was started in VNIIEF already in 1990 [7] in the form close to the Steinberg model [18]:

$$Y_S = Y_0 \cdot \left[\left(1 + \beta \cdot \varepsilon_i^p\right)^m + \alpha \cdot P\right] \cdot \left[1 - \frac{E_T}{E_{Tm}}\right], \tag{2.5}$$

where Y_0=0.35 GPa, Y_{max}=1.31 GPa, β=26.0, m=0.78, α=0.14 GPa^{-1} are constant coefficients; E_T is the current heat energy, which can be determined from the equation of state in the Mie-Grueneisen form, E_{Tm} is the heat energy, which is required for homogeneous heating of substance up to the melting temperature. It is determined from the Lindemann's law. This model is based only on experimental data, which were obtained by the method of main stresses [7]. It was used for description of beryllium state behind the shock wave front (Fig. 2.1).
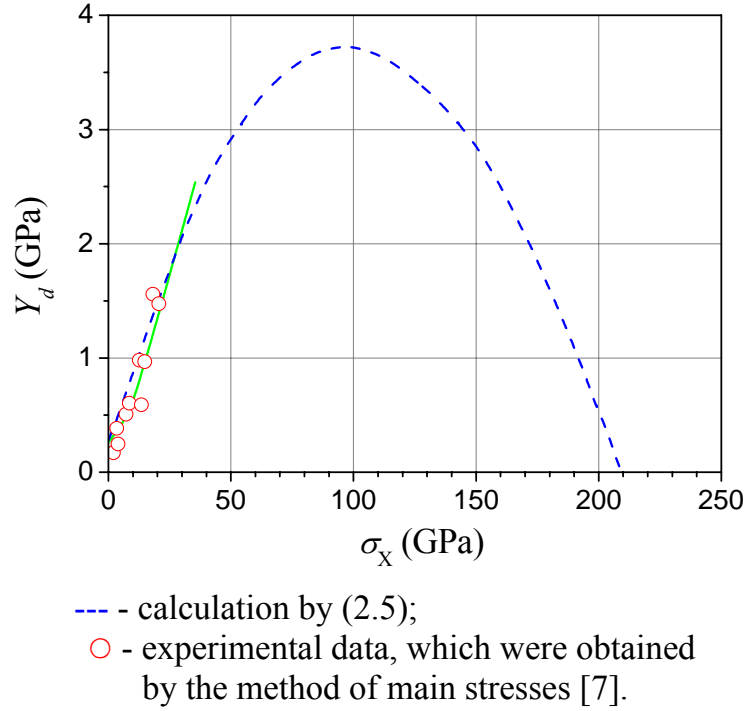
--- - calculation by (2.5);

○ - experimental data, which were obtained
by the method of main stresses [7].

Fig. 2.1 – Dynamic yield strength behind shock wave front for beryllium

2.4 Relaxation model of Steinberg

To describe planar deformation of *S-200E* beryllium in work [20], relaxation model
in the following form is suggested:

$$\dot{S}_1 = 2G\dot{\varepsilon} - \frac{S_1 - S_{eq}}{\tau},$$

$$\dot{S}_{eq} = 2G\dot{\varepsilon}, \text{ at } |S_{eq}| < \frac{2}{3}Y,$$

$$\tau = A_1 \cdot \exp\left(Q \middle/ E_{in}\right),$$

$$E_{in} = (E - E_c) + A_2|S\dot{\varepsilon}|,$$

(2.6)

where ε is the strain; G is the shear modulus; S_{eq} is the stress deviator, which is equilibrium
or independent on strain rate; Y is the strength limit; τ is the relaxation time; A_1, A_2, Q are
constant values. In work [20], basing on the conditions of the best description of profiles of
free surface velocity when loading beryllium by shock waves with intensity up to ~3 GPa,
the following parameters of equations (2.6) were selected: $A_1=10^{-14}$μs, $A_2=2$μs, $Q=214.3$.

3   Relaxation model of beryllium strength (RING)

Below we present the model of beryllium shear strength, which is under development in VNIIEF, and which was used in calculations [21]. The model parameters were selected basing on available experimental data. These data can be updated after obtaining new experimental information.

3.1 Equations of state

In the area of pressures lower than 100 GPa, the spherical component of stress tensor can be presented in the simplified Mie-Grueneisen form with constant heat capacity:

$$P = P_X(V) + \Gamma_P \cdot \rho \cdot C_V \cdot T \cdot D\left(\frac{\Theta}{T}\right),$$

$$E = \frac{C_{0K}^2}{n}\left[\frac{\delta^{n-1}}{n-1} + \frac{1}{\delta} - \frac{n}{n-1}\right] + E_T.$$

(3.1)

In relation (3.1), ρ_{0K}, C_{0K} are the density and volume sound velocity at T=0 °K; $\frac{\rho_{0K}C_{0K}^2}{n}(\delta^n - 1) = P_e$ is the elastic component of pressure; Γ_P is he Grueneisen coefficient; ρ is the substance density; $\delta = \frac{\rho}{\rho_{0K}}$ is the relative compression; $C_V = \frac{3R}{A}$ is the specific heat capacity at constant volume (the Dulong-Petit law); $D\left(\frac{\Theta}{T}\right)$ is the Debye function; Θ is the Debye temperature.

Because of high value of the beryllium Debye temperature (Θ=1031 K), its specific heat C_V is much lower than the value $\frac{3R}{A}$ at normal temperature, and it is a function of the current temperature. Respectively, specific heat energy is less than the value $\frac{3R}{A} \cdot T$, and it can be written as the following: $E_T = E_{T0} + \int_{T_0}^{T} C_V(T)dT$, where $E_{T0} = \int_{0}^{T_0} C_V(T)dT$ is the specific heat energy at normal temperatures. Calculations give the value E_{T0}=183 J/g.

The equations of state are based on the available data on measurement of the *D-U* diagrams of compression [22], sound velocity behind shock wave front [15], etc. [23]. The Grueneisen coefficient Γ_P is assumed as a function of only density (or relative compression (δ) [24]. It is true for not too high temperatures.

$$\Gamma_P = \Gamma_\infty + \frac{\Gamma_0 - \Gamma_\infty}{\delta^M},$$ (3.2)

where Γ_0 is the value of Γ_P at $\rho = \rho_{0K}$ and $\Gamma_\infty = \Gamma_P$ at $\delta \to \infty$.

The beryllium Grueneisen coefficient Γ_P is $\Gamma_0 = 1.15$, $\rho_{0K} = 1.86$ g/cm^3 under normal conditions according to [25].

Table 3.1 presents constant coefficients of equations (3.1) and (3.2) for beryllium. Parameters of the physical equation were selected to meet the conditions: $P=0$ at $\rho = \rho_0$, $T=273$ °K and $P=0$ at $\rho = \rho_{m0}$, $T=1557$ °K.

Table 3.1 - Constant coefficients of beryllium equations (3.1) and (3.2)

ρ_{0K} (g/cm^3)	ρ_0, (g/cm^3)	$C_{0K,}$ (m/s)	n	Γ_∞	Γ_0	M	c_V, (J/gK)
1.8668	1.85	8.03	2.89	0.5	1.25	1.0	2.7

3.2 Shear modulus and melting temperature

Shear modulus, which determines the deviator component of stress tensor in the elastic area of strain, is usually calculated by the formula:

$$G = \frac{3}{2} \cdot \frac{1-2\nu}{1+\nu} \cdot \rho \cdot C_K^2, \qquad C_K^2 = \left(\frac{\partial P}{\partial \rho}\right)_S,$$ (3.3)

where ν is the Poisson's ratio; C_K is the current volume sound velocity.

The dependence of the Poisson's ratio ν can be assumed as a function of temperature $\nu\,(T/T_m)$. And it can be presented in the linear or power forms:

$$\nu = \nu_0 \cdot \left(1 + C \cdot \left(\frac{T}{T_m}\right)^K\right), \ \bar{T} < 1$$ (3.4)

$\nu = 0.5,\ T \geq 1,$

where $\bar{T} = \dfrac{T}{T_m}$, T is the current temperature; T_m is the melting temperature, ν_0, C, K=const.

At the shock wave front, the Poisson's ratio can be determined using the relation of elastic sound velocity C_L and volume sound velocity C_K:

$$v = \frac{3C_B^2 - C_L^2}{3C_B^2 + C_L^2}$$

(3.5)

Table 3.2 presents parameters for the dependence of the Poisson's ratio on temperature in form (3.4).

Table 3.2 – Parameters of equation (3.4)

v_0	C	K
0.03	15.63	3.0

Formula (3.4) describes the reference value $v = v_0 = 0.03$ at $T = 300\,°K$, and $v = 0.5$ at $T = T_m$ that corresponds to the liquid state. To obtain the more justified dependence $v = f(\rho, \bar{T})$, it is required to have additional experimental data. After obtaining additional experimental information, it is possible to revise the dependence $v = f(\rho, \bar{T})$ and the parameters. Fig. 3.1 shows calculated and experimental data [15], [16] on elastic C_L and plastic C_B sound velocities behind the shock wave front.

— calculation of C_L;
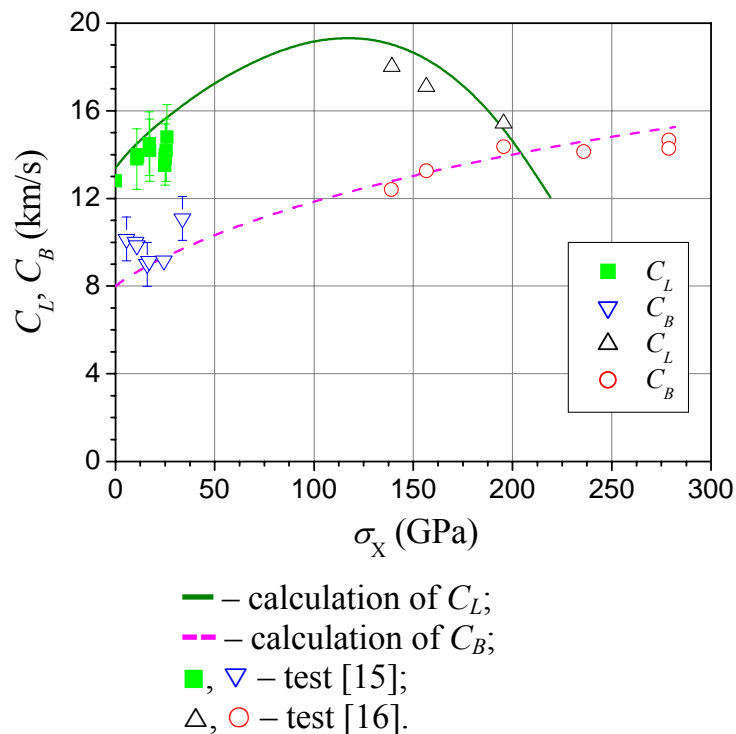— calculation of C_B;
■, ▽ — test [15];
△, ○ — test [16].

Fig. 3.1 - Calculated and experimental dependences of elastic C_L and plastic C_B sound velocities on pressure behind shock wave front

In the specified stress-strain state, the melting temperature T_m is determined by the Lindemann's law:

$$\frac{d \ln T_m}{d \ln \rho_m} = 2\left(\Gamma_p - \frac{1}{3}\right),$$

where T_m is the melting temperature at density ρ_m.

At the initial conditions $T_m = T_{m0}$, $\rho_m = \rho_{m0}$, the melting curve equation in the *(δ-T)* plane has the form:

$$T_m = T_{m0}\left(\frac{\delta_m}{\delta_{m0}}\right)^{2\left(\Gamma_\infty - \frac{1}{3}\right)} \exp\left[\frac{2(\Gamma_0 - \Gamma_\infty)}{M}\left(\frac{1}{(\delta_{m0})^M} - \frac{1}{(\delta_m)^M}\right)\right], \qquad (3.6)$$
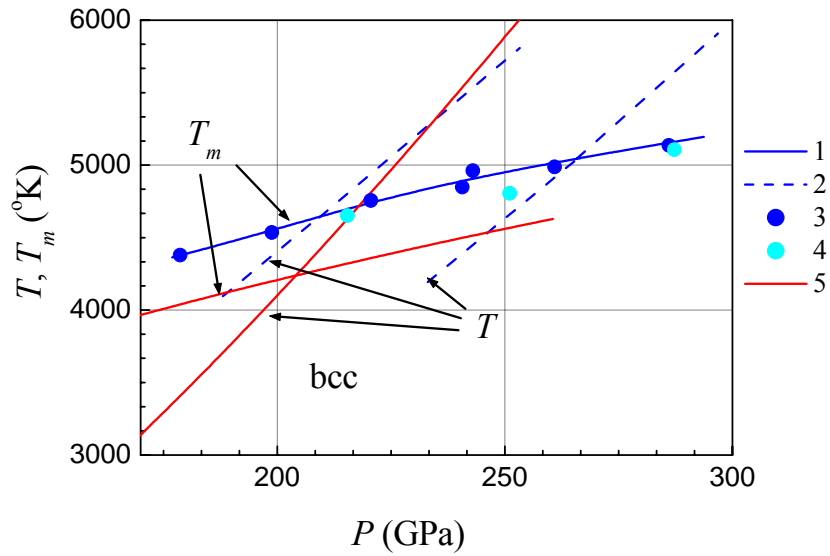
where $\delta_m = \dfrac{\rho_m}{\rho_{0K}}$, $\delta_{m0} = \dfrac{\rho_{m0}}{\rho_{0K}}$ is the relative density of substance at $T_m = T_{m0}$, (the melting beginning), T_{m0} is the melting temperature in the normal state at $P \approx 0$. For beryllium, $T_{m0} = 1557$ °K, $\delta_{m0} = 0.9145$.

Fig. 3.2 shows calculated and available experimental dependences of temperature and melting temperature.
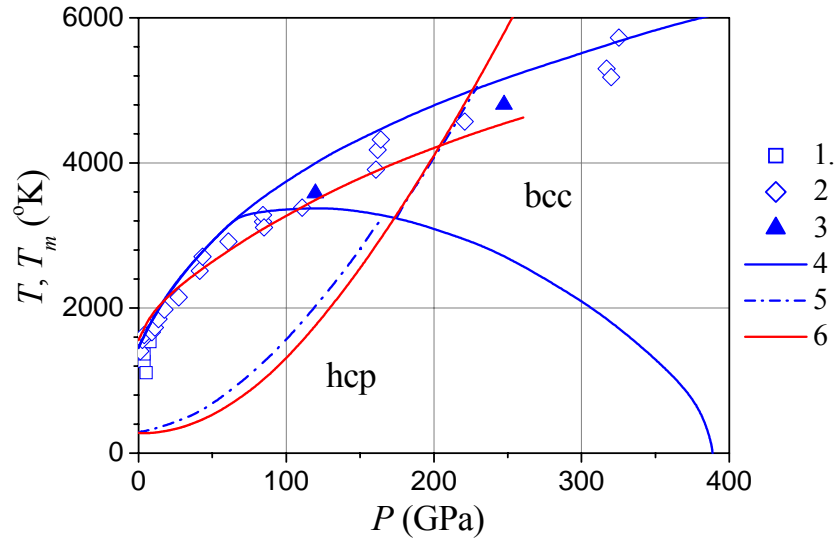
1-3 – data from [26];
4,5 – calculation from [26];
6 – calculation by formulas (3.1) - (3.6).

a)

1-4 – data from [27];
5 – calculation by formulas (3.1)-(3.6).

b)

Fig. 3.2 – Experimental and calculated dependences of temperature and
melting temperature along shock adiabat of beryllium

3.3 Relaxation model RING-I

For more complete description of metal behavior at high-rate deformation, including shock-wave deformation, relaxation models of elastic-plastic body are used. In these models, it is expected that the stress deviator depends on deviators of deformations and strain rates [28].

VNIIEF experts are using a simplified relaxation model, which involves usual elastic-plastic approximation, and dynamic yield strength is determined by differential equation, which takes account for the process of relaxation of elastic stress. The basic equation, which determines the effective yield strength in the relaxing media, is the following:

$$\dot{Y}_d = 3G\dot{\varepsilon}_i - \frac{Y_d - Y_S}{\tau},\qquad(3.7)$$

where Y_d is the effective yield strength at present time; Y_S is the stationary yield strength, which occurs in present state *(P, T)* of substance at $\dot{\varepsilon}_i = 0$; $\dot{\varepsilon}_i$ is the strain rate; τ is the relaxation time for elastic stress. Points above Y_d and ε_i mean the derivative in time. When yield strength $\left(\dot{Y}_d \cdot \tau << Y_d\right)$ changes rather slow, equation (3.7) turns to elastic-viscous-plastic model.

The stationary yield strength is presented in the following analytical form:

$$Y_S = Y_0 \cdot \left[1 + \left(a_1 \cdot (1 - \overline{T}^{\,a_3})\right) \cdot \left(1 - \exp\left(-a_2 \cdot \left(\int_0^t \varphi_1(\dot{\varepsilon}_i) \cdot \dot{\varepsilon}_i dt\right)\right)\right)\right] \cdot \frac{G}{G_0}$$

$$\varphi_1 = \frac{1 + \varphi_{max1} \cdot \left(\dfrac{\dot{\varepsilon}_i}{\dot{\varepsilon}_{1S}}\right)^{a_4}}{1 + \left(\dfrac{\dot{\varepsilon}_i}{\dot{\varepsilon}_{1S}}\right)^{a_4}}\qquad(3.8)$$

In equation (3.8), Y_0, a_1-a_4, φ_{max1}, $\dot{\varepsilon}_{1S}$ are constant coefficients. This equation takes account for the loading history, i.e. the dependence of hardening on strain rate and value of strain [6]. Table 3.3 presents the parameters of equation (3.8).

Table 3.3 – Parameters of stationary yield strength of beryllium

Y_0 (GPa)	a_1	a_2	a_3	a_4	φ_{max1}	$\dot{\varepsilon}_{1S}$ (s^{-1})
0.36	3.3	7.0	1.0	1.0	2.0	2.0

For relaxation time, the equation is used, which describes the tests with measurement of strain rate [14], [29] in shock wave front, and compression diagrams and Taylor cylinders at $\dot{\varepsilon}_i < 10^5$ s^{-1}:

$$\tau = \frac{\tau_0 \cdot \left(1 - \overline{T}\right)^2}{\dfrac{G}{G_0} \cdot \left(1 + \dfrac{\dot{\varepsilon}_i}{\dot{\varepsilon}_{i0}} \cdot \varphi_2\left(\dot{\varepsilon}_i\right)\right)^{0.5}}, \text{ where} \tag{3.9}$$

$$\varphi_2\left(\dot{\varepsilon}_i\right) = \frac{1 + \varphi_{max2} \cdot \left(\dfrac{\dot{\varepsilon}_i}{\dot{\varepsilon}_{2S}}\right)^{n_2}}{1 + \left(\dfrac{\dot{\varepsilon}_i}{\dot{\varepsilon}_{2S}}\right)^{n_2}}. \tag{3.10}$$

Equation (3.9) has the following limiting values:

$G = G_0$ $\tau = \tau_0$ at $\dot{\varepsilon}_i \to 0$, and (or) $\dot{\varepsilon}_i \to \infty$, $\tau \to 0$ at $\overline{T} \to 1$.

With the parameters $\varphi_{max2} = 5$; $n_2 = 1.0$, $\dot{\varepsilon}_{2S} = 2 \cdot 10^3$ s^{-1}, $\tau_0 = 5$ μs and $\dot{\varepsilon}_{i0} = 1$ s^{-1}, the dependence in form (3.9) is in rather good agreement with experimental data up to strain rate $\dot{\varepsilon}_i \sim 10^8$ s^{-1}.

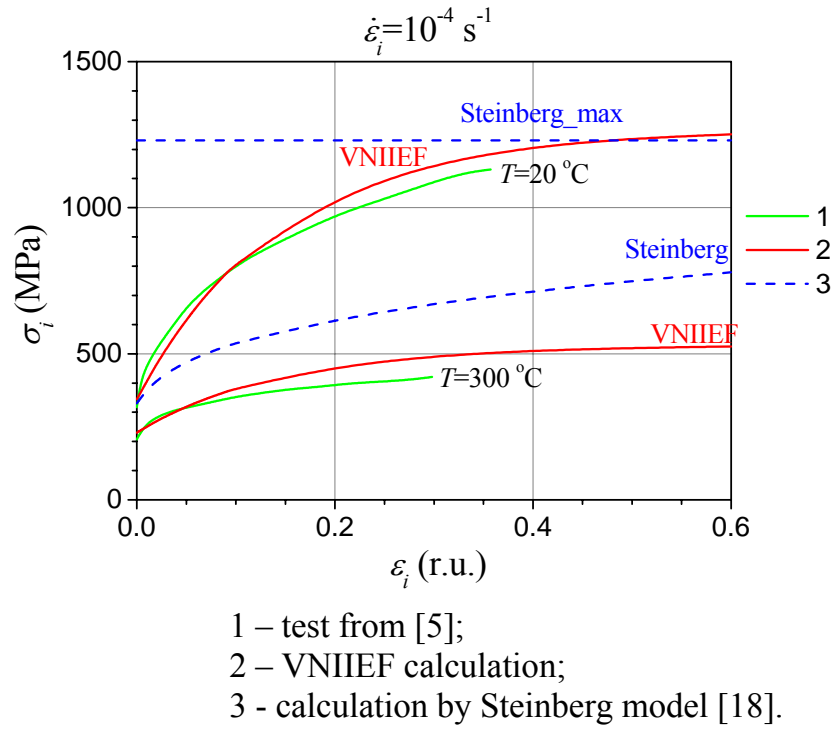Below, Fig. 3.3-Fig. 3.5 present results of description of the available experimental data by the model.

$\dot{\varepsilon}_i = 10^{-4}\ s^{-1}$

Steinberg_max

VNIIEF

T=20 ^{o}C

1

Steinberg

2

3

VNIIEF

T=300 ^{o}C

1 – test from [5];
2 – VNIIEF calculation;
3 - calculation by Steinberg model [18].

Fig. 3.3 – Experimental and calculated σ-ε diagrams of beryllium compression at T=20 °C, T=300 °C and strain rate $\dot{\varepsilon}_i$ =2·10^{-4} s^{-1}

$\dot{\varepsilon}_i = 1\text{-}2\ s^{-1}$

T=20 ^{o}C

VNIIEF 20 ^{o}C

Steinberg_max

T=200 ^{o}C

VNIIEF 200 ^{o}C

Steinberg 20 ^{o}C

T=300 ^{o}C

VNIIEF 400 ^{o}C

T=400 ^{o}C

1

2

3

4

1 - test from [5];
2 - test from [6];
3- calculation by Steinberg model [18];
4 - VNIIEF calculation.
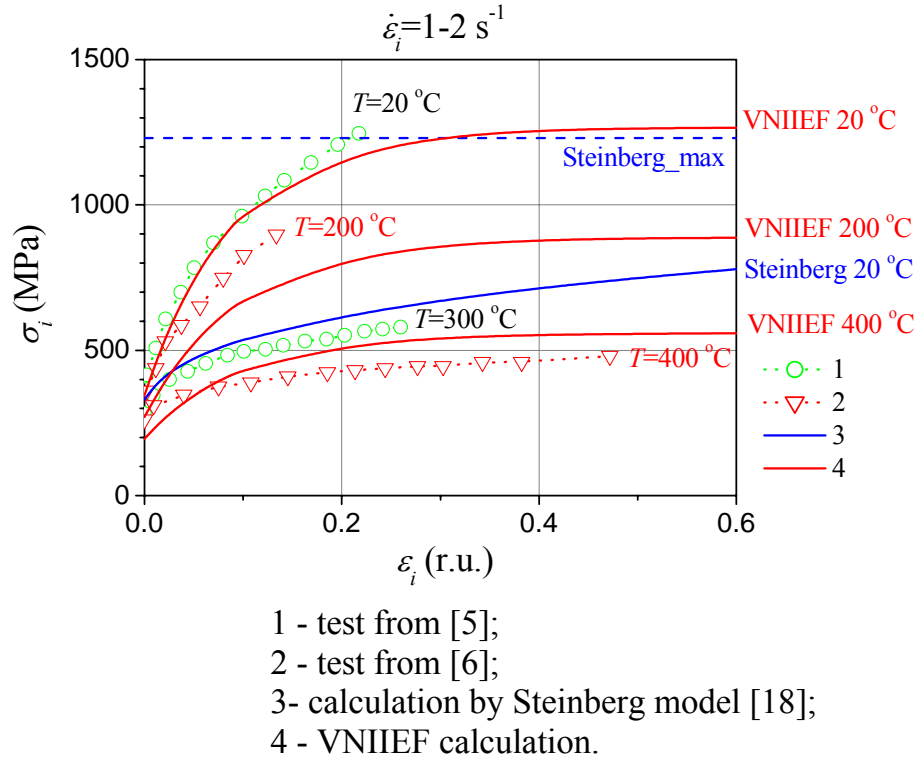
Fig. 3.4 – Experimental and calculated σ-ε diagrams of beryllium compression at T=20 °C, T=200 °C, T=300 °C, T=400 °C and strain rate $\dot{\varepsilon}_i$ =1-2 s^{-1}

1 – test from [6];
2 – test from [7];
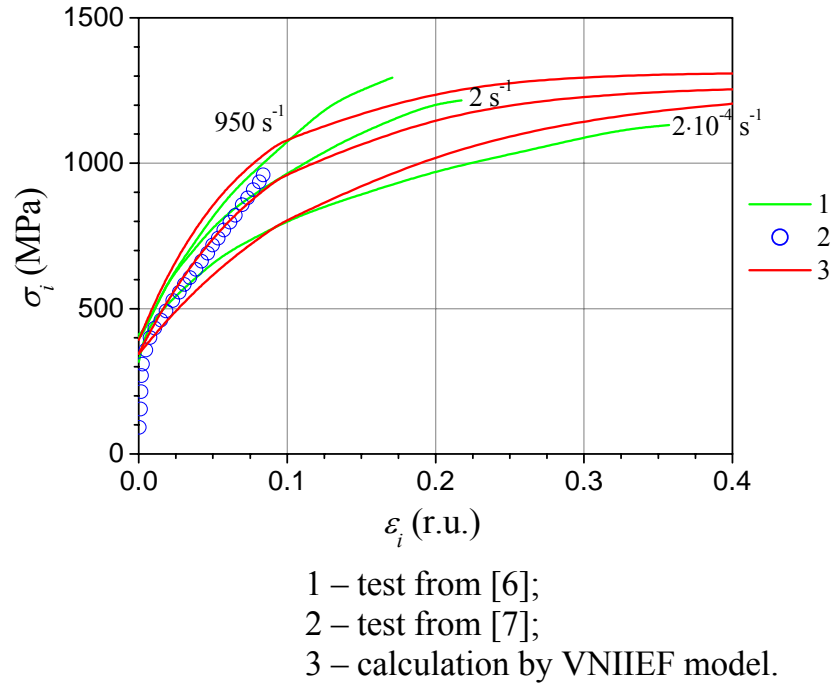3 – calculation by VNIIEF model.

Fig. 3.5 – Experimental and calculated σ-ε diagrams of beryllium compression at T=20 °C and various strain rates

Calculated and experimental dependences of yield strength on temperature at various strains are shown in Fig. 3.6.
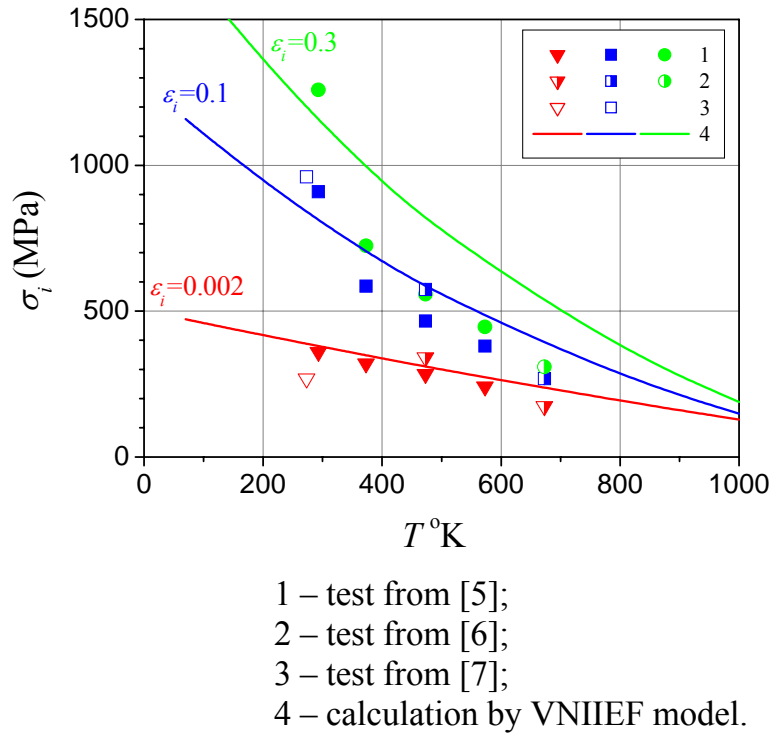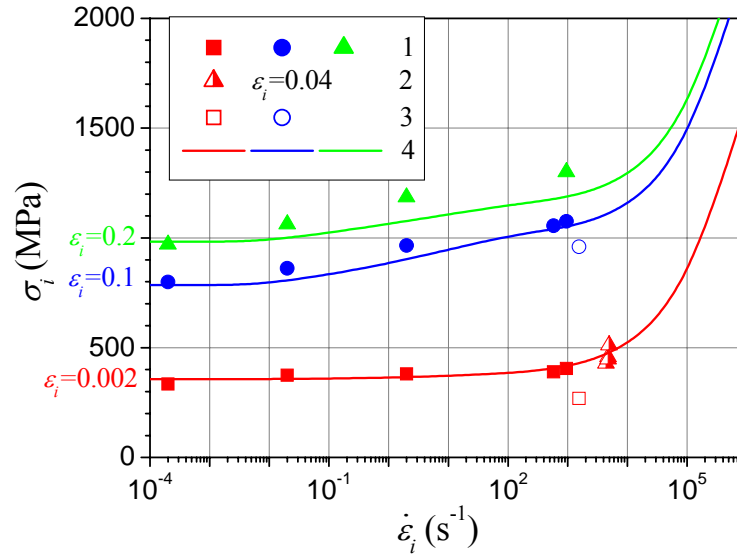

1 – test from [5];
2 – test from [6];
3 – test from [7];
4 – calculation by VNIIEF model.

Fig. 3.6 - Calculated and experimental dependences of stress intensity on temperature at various strains and $\dot{\varepsilon}_i$ =2·10^{-2}s^{-1}

The suggested form of beryllium yield strength allows getting rather correct description of the experimental dependences of dynamic strength on strain.

Fig. 3.7 and Fig. 3.8 show dependences of stress intensity on strain rate at various strains ε_i=0.002, ε_i=0.1, ε_i=0.2 and temperatures.

1 - test from [5];
2 - test from [6];
3 - test from [7];
4 - calculation.

Fig. 3.7 - Calculated and experimental dependences of yield strength
on beryllium strain rate at various strains and T=20 °C

1 - test from [5];
2 - calculation.
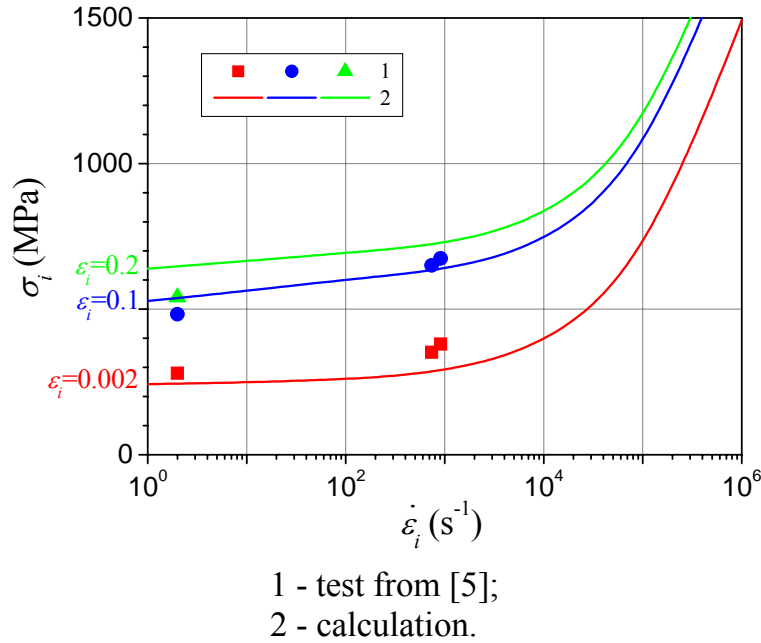
Fig. 3.8 - Calculated and experimental dependences of yield strength on beryllium strain rate at various strains and *T*=300 °C

Here we would like to note the nontrivial fact of yield strength growth at $\dot{\varepsilon}_i \sim 2$ s^{-1} and $\varepsilon_i^p > 0.1$. It is, probably, associated with formation of a large number of twins at this loading regime. This fact is taken into account in the model.

Table 3.4 presents the results of simulation of experimental data, which were obtained by the Taylor method [8].

Table 3.4 – Results of simulation of tests with *S-200* beryllium by the Taylor method

W_{imp} (m/s)	158	181	203	205	273
(L_f/L_0) calc	0.96	0.95	0.943	0.942	0.92
(L_f/L_0) exp	0.970	0.963	0.958	0.953	0.932
$\dfrac{L_f\, calc}{L_f\, exp}$	0.990	0.989	0.984	0.989	0.987

It follows from Table 3.4 that the calculated post-test lengths of cylindrical samples $L_{f\rho}$ and experimental $L_{f\ni}$ are in good agreement. The systematic small difference between them, which is equal to (1÷1.6) %, is, probably, associated with difference in the manufacture technologies.

In work [13] (data of Yu.I. Meshcheryakov), profiles of elastic precursor and plastic wave were recorded when loading beryllium by shock waves. Results of description of the available experimental data by the RING-I model are presented in Fig. 3.9.
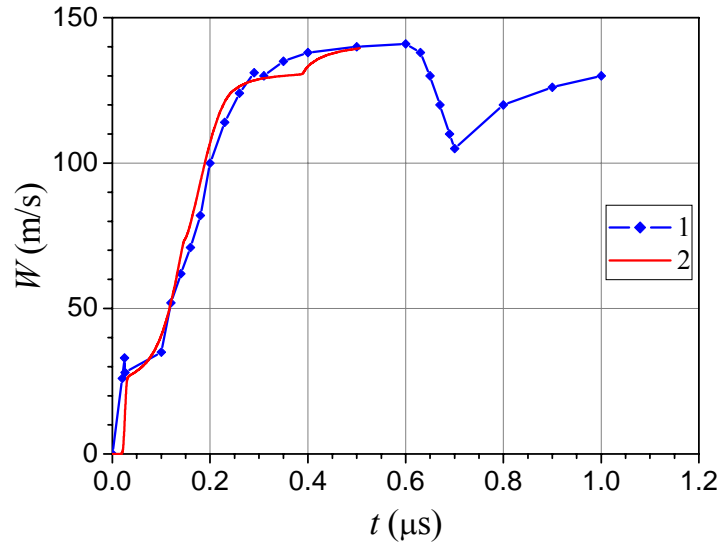
1 – test from [13];
2 - calculation (Δ_S=3.96 mm, Δ_{imp}=1.88 mm,
W=147.3 m/s, impactor made of *D-16*).

Fig. 3.9 - Dependence of free surface velocity on time for *Be*

Fig. 3.10 shows the calculated dependence of beryllium strain rate on pressure in shock wave front. Also it presents the experimental values.
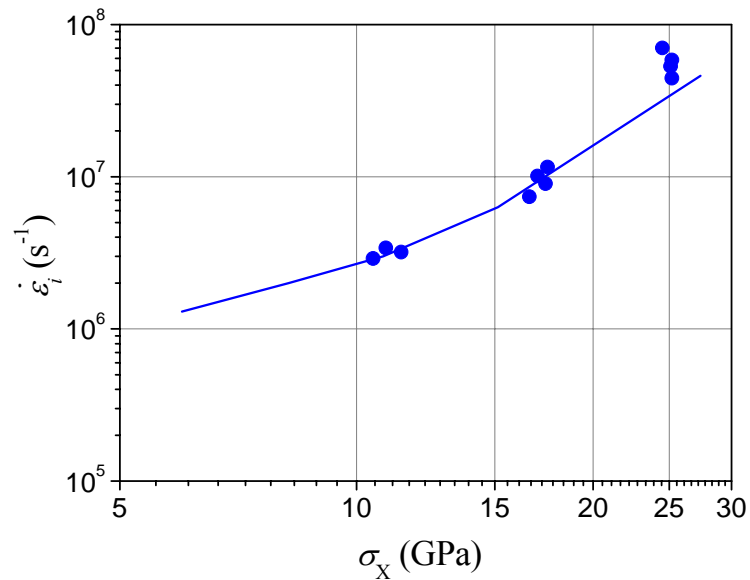
1 – test from [14];
2 - calculation.

Fig. 3.10 – Dependence of strain rate on loading intensity
in shock wave front

4   Results of velocity measurements of liners accelerated by two-stage loading device

Association between perturbation growth and shear strength is determined basing on numerical simulation. It is very important to provide reliable description of the liner loading regime, in particular, the $P(t)$ dependence. Error of $P(t)$ calculation can be caused by inaccuracy of the equation of state of HE detonation products.

To verify reliability of the $P(t)$ calculation, measurements of the dependence of velocity of vanadium liner free surface on time were performed [3], [4]. The measurements were performed by Fabry-Perot laser interferometer [30]. Beside Fabry-Perot interferometer, VISAR and radiointerferometer were used for the liner velocity measurements. The $W(t)$ dependence of velocity on time is mostly determined by pressure of explosion products on loaded surface and by equation of state of vanadium. Numerical description of $W(t)$ gives grounds to believe that $P(t)$ is also correctly calculated.

Measurements of the dependence of the beryllium liner free surface velocity on time will be performed at Task 2 of the Agreement.

4.1   Measurements of vanadium liner velocity

Fig. 4.1 presents a scheme of the experimental assembly intended for measurement of vanadium liner velocity, which was earlier published in works [3], [4].

Explosion products of HE charge of the first stage accelerated a steel impactor through a plexiglass damper. It provided the regime of overcompressed detonation in HE of the second stage. Explosion products of HE of the second stage loaded quasi-isentropically (without formation of shock waves) the vanadium liner. The liner flight basis V was 18.5 mm, and it was limited by a cutoff made of plexiglass with the sizes $\varnothing 120 \times 10$ mm. When performing the test, the assembly was vacuumized to the residual pressure of 50 mm *Hg*.
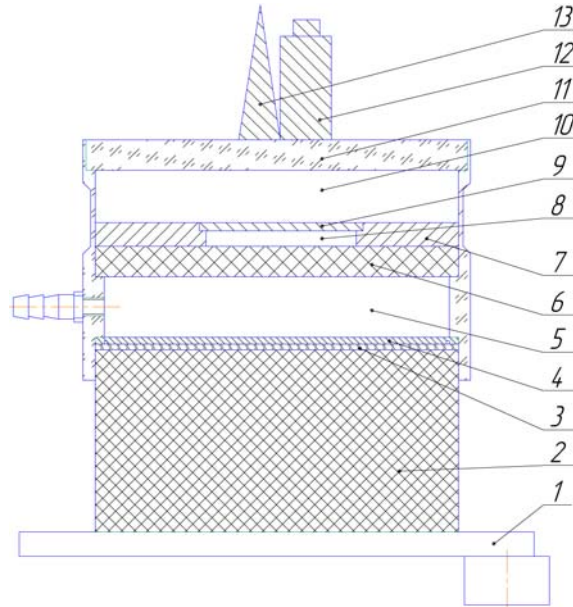
1 - generator of planar shock wave;
2 - HE of first stage: $\varnothing 120 \times 60$ mm;
3 - damper: plexiglass, $\varnothing 120 \times 2$ mm;
4 - impactor of first stage: *Fe*, $\varnothing 120 \times 2.2$ mm;
5 - vacuumized gap: $\delta = 20$ mm;
6 - HE of second stage: $\varnothing 120 \times 10$ mm;
7 - cartridge *Fe*, $\varnothing 120 \times 8$ mm;
8 - vacuumized gap: $\delta = 3$ mm;
9 - studied liner: *Be*, $\varnothing 50 \times 1.56$ mm;
10 – liner flight basis: *L*=18.5 mm;
11 - plexiglass (cutoff): $\varnothing 126 \times 10$ mm
12 - optical gauge
13 – gauge of radiointerferometer.

Fig. 4.1 – Experimental assembly

Gauges of the measuring techniques of laser interferometers (Fabry-Perot and VISAR) and radiointerferometer were mounted at equal distances from the vanadium liner center at the diameter of 20 mm. Using these techniques, profiles of velocity $W(t)$ and motion $X(t)$ were measured.

Fig. 4.2, Fig. 4.3, Fig. 4.4 present results of measurements of vanadium liner velocity, which were obtained with use of Fabry-Perot laser interferometer, VISAR (Michelson) и radiointerferometer, respectively.
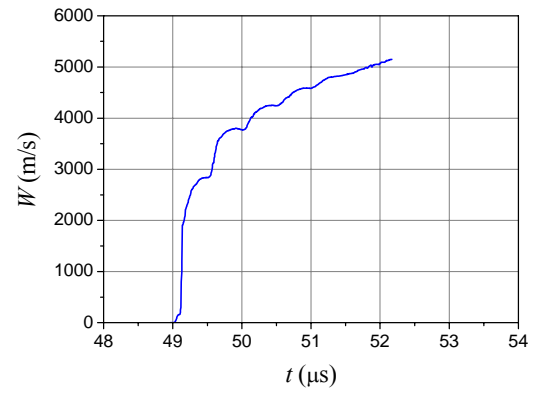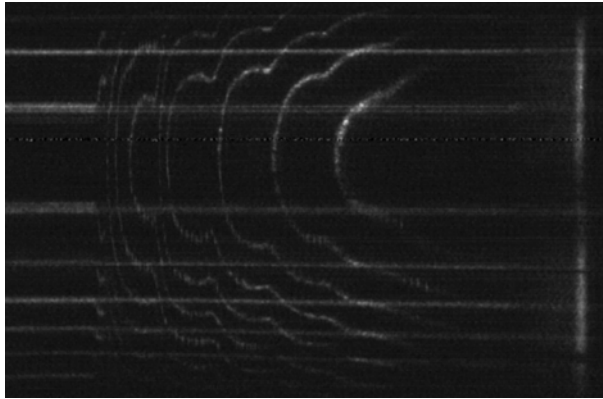

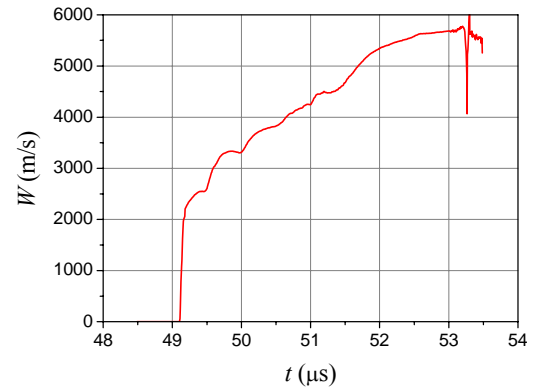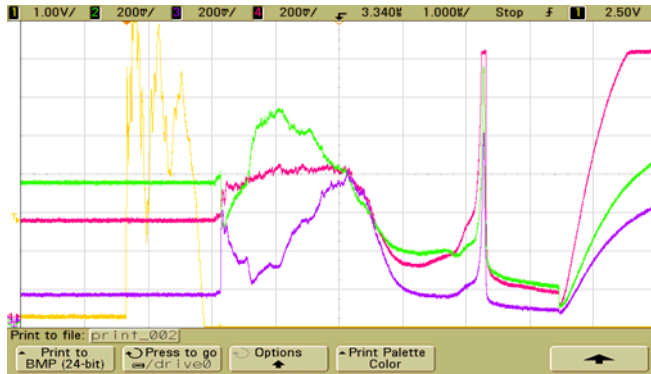Fig. 4.2 - Results of velocity measurement by Fabry-Perot interferometer

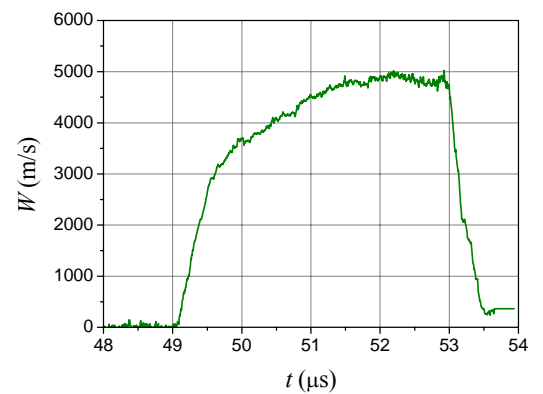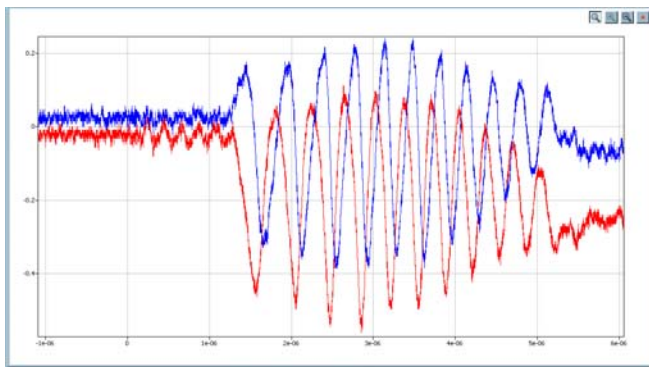Fig. 4.3 - Results of velocity measurement by Michelson interferometer

Fig. 4.4 - Results of velocity measurement by radiointerferometer

Generalization of the recorded dependences of the liner motion velocity is presented in Fig. 4.5.
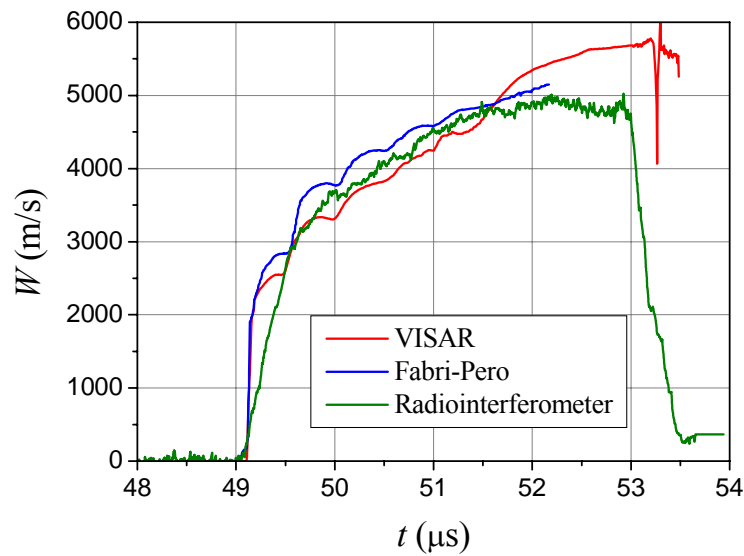

Fig. 4.5 – Generalized results of velocity measurements

The results, which were obtained with use of three independent methods of recording, have qualitative and quantitative differences. The velocity profiles, which were recorded by optical interferometers of Fabry-Perot and VISAR, are in qualitative agreement. Though the quantitative characteristics differ by the value up to 330 m/s. At the velocity profile, which was recorded by radiointerferometer, there are qualitative differences in dynamics of the liner acceleration. They are caused by absence of the first stage and insignificantly-expressed subsequent stepwise increase of velocity. This qualitative difference in liner acceleration dynamics, which was obtained by radiointerferometer, can be a consequence of differentiation of the experimentally recorded dependence of the liner motion on time, which is the basis of this method. In the time range $t=50 \div 51.5$ µs, scatter of velocities, which were obtained by all techniques, does not exceed 10 %.

5 Experimental setup for tests with investigation of dynamic strength of S200F beryllium

5.1 X-ray pulse technique. Liner design

To investigate shear strength of *Be* when loading it up to pressures P≈50 GPa, the dynamic method of perturbations is used [1], [2]. Fig. 5.1 presents the suggested scheme of test conduction. It was earlier used in [3].
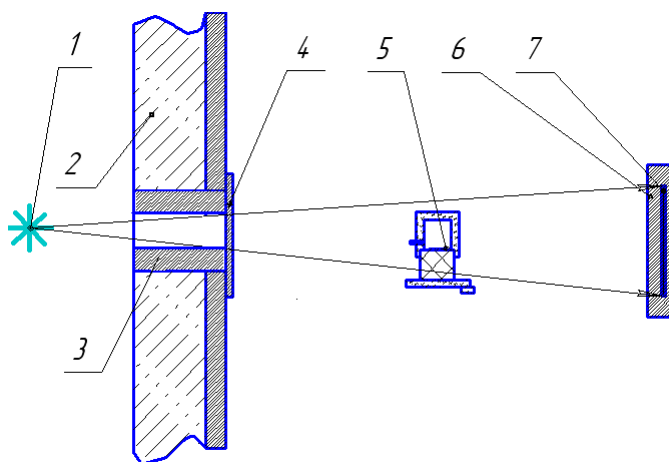
1 – source of X-ray radiation
2 – element of concrete wall of bunker
3 – collimator
4 – metal protective screen
5 – experimental assembly
6 – armored cassette
7 – screens ADC – CR (10 units).

Fig. 5.1 – Scheme for conduction of tests

Facility «Eridan-3» is the source of X-ray radiation. Its boundary radiation energy is 1 MeV, pulse duration at half-height is ~0.15 μs.

Information on perturbation growth is obtained basing on X-ray image of the investigated liner free surface. Recording of X-ray image is performed at the package of photochromic screens ADC - CR [31]. Images, which were obtained in the screens, are summarized by special algorithm [31]. Mathematical processing of the images is performed by the package of programs [32], [33].

Application of photochromic screens allows to provide two-frame recording at the same carrier because of width of their dynamic range (to expose the same package of screens by two X-ray pulses). Application of photochromic screens *in a package* allows to improve quantum efficiency (sensitivity) of the recording system, and, due to it, to reduce quantum fluctuations (noises) of X-ray images.

To perform tests with investigation of *Be* shear strength, it is suggested to use liners, where periodic perturbations are specified. The perturbations are periodically-located extended triangle-shaped recesses (grooves) in surfaces of the liners. The perturbations are prepared by milling. Order of recesses determines perturbation wave length λ, and depth determined the initial amplitude A_0 (amplitude $A_0=2a_0$, a_0 is a traditionally used designation of amplitude at harmonically varied function). Selection of parameters of the initial perturbations is performed basing on preliminary numerical calculations. To improve informativity of the tests, it is possible to use liners with two zones of initial parameters of perturbations.

Fig. 5.2 presents a scheme of the liner with perturbations. Similar designs of liners were earlier used in work [3]. Arrows show the loading direction.
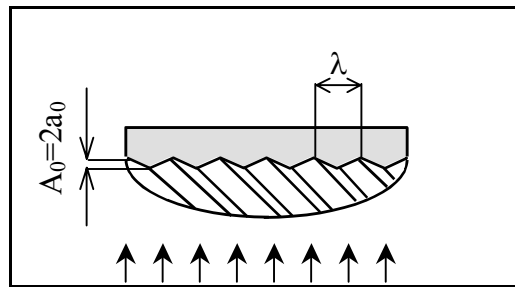

Fig. 5.2 - Scheme of investigated liner

Design of the *Be* liner was chosen basing on numerical simulation. Calculations were performed by one-dimensional [34] and two-dimensional codes [35]. Goal of the calculations was search for optimum geometry of the beryllium liner, which would provide the condition that its bending does not exceed the experimental error of the absolute perturbation amplitude measurement when its flight basis is 0÷10 mm at shock-wave or quasi-isentropic loading regimes in the pressure range $P\sim30\div60$ GPa. Currently the maximum error of the X-ray radiography method of perturbations is considered as a value not higher than 0.1 mm. The possible design of *Be* liner is presented in Fig. 5.3.
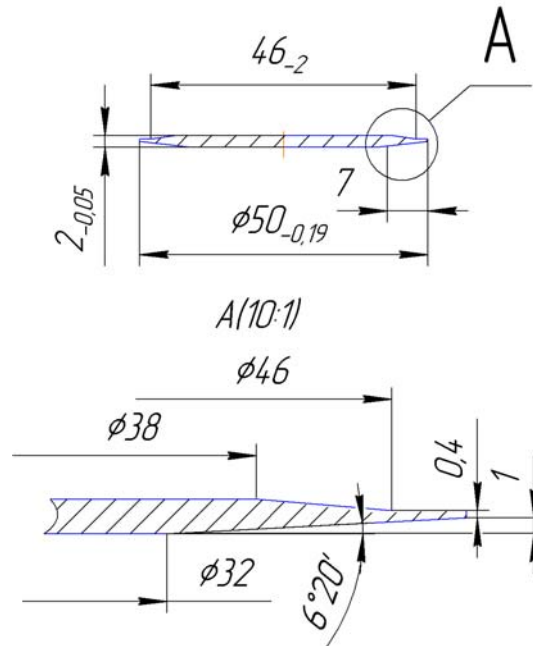
Fig. 5.3 - Design of *Be* liner

Configuration of the liner is selected basing on two-dimensional calculations. The chosen shape provides absence of screening of the central zone of liner by edges. In the chosen design, edges are moving a bit faster than the central zone. The calculated liner shape is presented at the flight base *S*=10 mm in Fig. 5.4
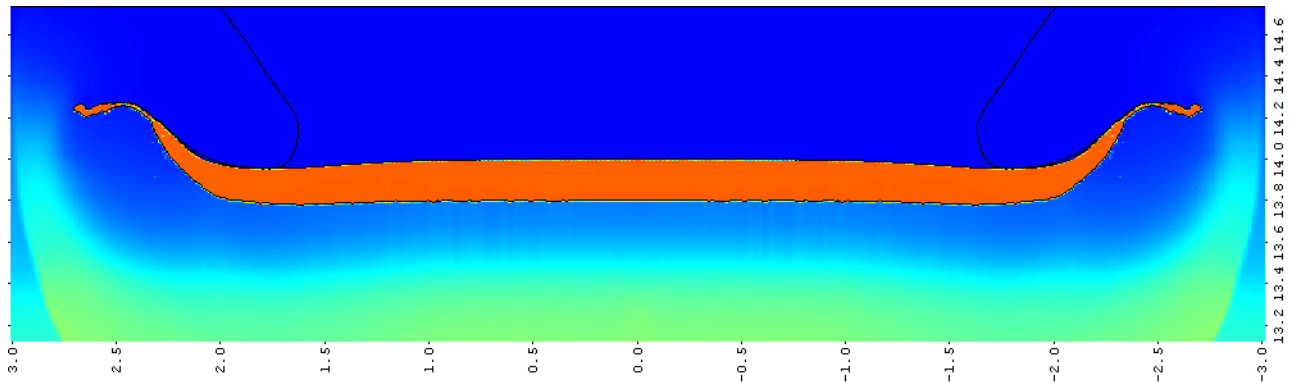

Fig. 5.4 - Shape of liner at the flight base *S*=10 mm

Fig. 5.4 shows that actually there are no any liner bends at *S*=10 mm. The liner edges are flying ahead, and it provides reliable X-ray radiography recording with minimum error in measurements of perturbation amplitude.

5.2 Experimental setup

To investigate *Be* shear strength by perturbation method in the pressure area up to *P*≈50 GPa and strain rates up to $\dot{\varepsilon} \sim 10^6 s^{-1}$, it is suggested to use the experimental assembly, which was earlier used in work [3]. Scheme of the assembly is presented in Fig. 5.5.

Vacuumized gap of 2 mm between the investigated liner and HE cartridge of the second stage provides quasi-isentropic (shockless) loading of *Be* liner. HE with caloricity *Q*=6.1 KJ/g is used in the tests.
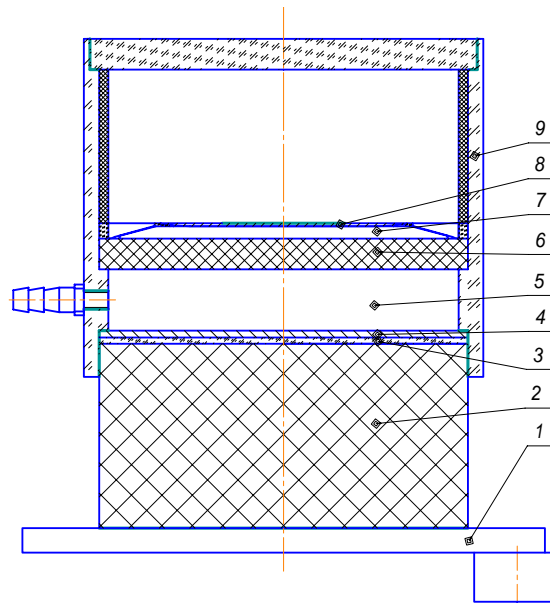
1 - generator of planar shock wave;
2 - HE of first stage: $\varnothing 90 \times 80$ mm;
3 - damper: plexiglass, $\varnothing 90 \times 2$ mm;
4 - impactor of first stage: *Fe*, $\varnothing 90 \times 2.2$ mm;
5 - vacuumized gap: δ=10 mm;
6 - HE of second stage: $\varnothing 90 \times 10$ mm;
7 - vacuumized gap: δ=2 mm;
8 - studied liner: *Be*, $\varnothing 50 \times 2$ mm;
9 - sealing cylinder.

Fig. 5.5 - Two-stage loading device for quasi-isentropic loading of *Be* liner. *P*≈50 GPa

Fig. 5.6 presents the calculated dependences of loading pressure, velocity and displacement of the loaded surface of the investigated liner on time.
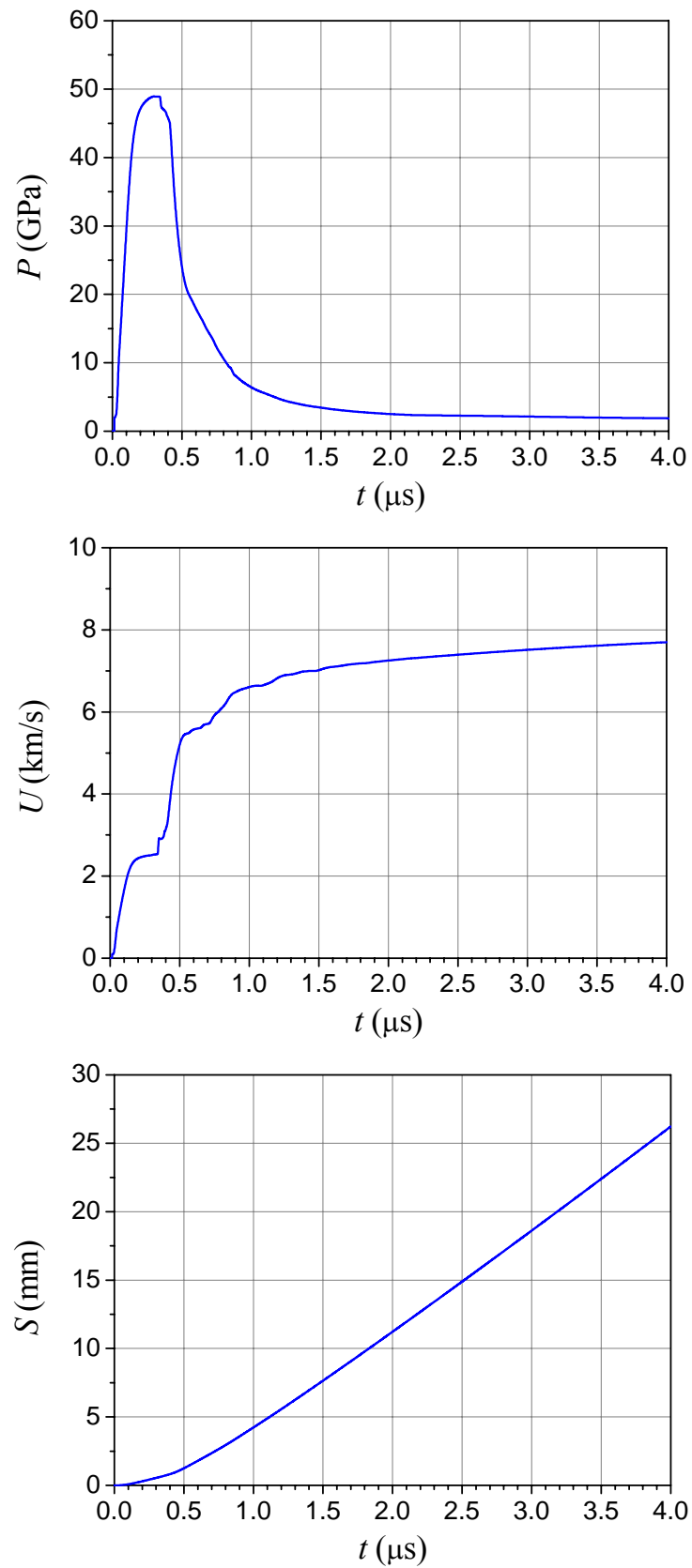
Fig. 5.6 - Time dependences of loading pressure, velocity and displacement of loaded surface of investigated *Be* liner under quasi-isentropic loading. *P*≈50 GPa

According to estimations, when loading the liner, strain rate in compression wave is $\dot{\varepsilon}_i \sim 10^6$ s^{-1}. Increment of thermal energy is $\Delta E_T \approx 416$ J/g after deformation. Under normal conditions, thermal energy of *Be* is $E_T \approx 547$ J/g. Thermal energy in the beginning of melting is $E_m \approx 2846$ J/g. Therefore, thermal energy of *Be* after deformation is $\approx 34\,\%$ of melting energy E_m. Increment of thermal energy regarding to the energy required for heating from the initial state to melting is $\dfrac{\Delta E_T}{E_m - E_T} \approx 0.18$.

6 Justification of experimental setup for tests with perturbation growth recording

Numerical prediction of the scheduled tests was performed by the two-dimensional Lagrangian technique DRAKON, which was earlier used in works [3], [35], with use of the phenomenological model of shear strength RING (see section 3). Compression hardening of metal, thermal softening due to heating, as well as strain hardening, which corresponds to static loading, are taken into account in the frames of this model. The model presents the dependence of dynamic yield strength on strain rate. It increases applications of this model, namely, as compared to the stationary model, opportunity appears to describe the phenomenon of attenuation of elastic precursor, width of shock wave front. It should be noted that the primary experimental information, which was required for verification of the phenomenological strength model, was obtained mainly from specific tests, which were directly intended for investigation of dynamic strength, where influence of the other factors (compressibility, uncertainty in EOS of HE, etc.), was insufficient. The perturbation method is one of such methods. It allows determining the occurred strength in test by describing results of experimental X-ray radiography by calculation.

Table 6.1-Table 6.4 present spatial distributions of pressure and rheological characteristics in sample during instability growth on surface of accelerated liner. It is possible to see in the presented calculation results that intensive perturbation growth is observed up to the flight base of ~6 mm. Then it is possible to observe drop of accelerating pressure due to chemical HE explosion products, and growth of both the perturbation amplitude and plastic strain is significantly decreased in the middle zone of the sample. All process of deformation takes place at the characteristic strain rate of $\sim 10^5 \div 10^6$ s^{-1}.

Fig. 6.1 presents results of calculations of periodically-extended perturbation growth on the liner surface with the following parameters: wavelength is λ=2mm; the initial amplitudes of perturbations are A_0=0.25, 0.3, 0.35, and 0.4 mm. It is possible to see in the presented graphs that a stable evolution regime occurred for lowest amplitude in the conditions of work of the two-stage loading system. The average value of shear strength in the sample area, which is responsible for plastic deformation during instability growth, is from 1.5 to 2 GPa. Accumulation of significant level of plastic deformation occurs due to perturbation growth. The calculation results from Fig. 6.2 show that, starting from the flight base of 6 mm, sample transition to the elastic state takes place and plastic strain accumulation stops. In accordance with various opinions on metal destruction during intensive plastic flow (the Gurson model [36]), destruction at shear strains should take place, since their amplitude exceeds significantly the critical value in the elastic state.

Taking account for the fact that beryllium shows brittle and anisotropic character of deformation in the normal conditions, the scheduled tests can significantly extend the scope of experimental information on dynamic shear strength and plasticization of beryllium in shock waves.

Basing on result of preliminary calculations, it is suggested to perform the first series of tests for investigation of dynamic strength of beryllium at shockless loading up to 50 GPa with initial amplitudes A_0=0.25 and 0.35 mm with two-frame X-ray recording of the instability growth process at liner flight bases of 5 and 10 mm. The final choice of the initial parameters and times of X-ray radiography will be coordinated with LLNL representatives (R. Covallo).

Table 6.1 - Spatial distributions of accumulated plastic strain in sample versus traveled distance (λ=2 mm, A_0=0.35 mm)

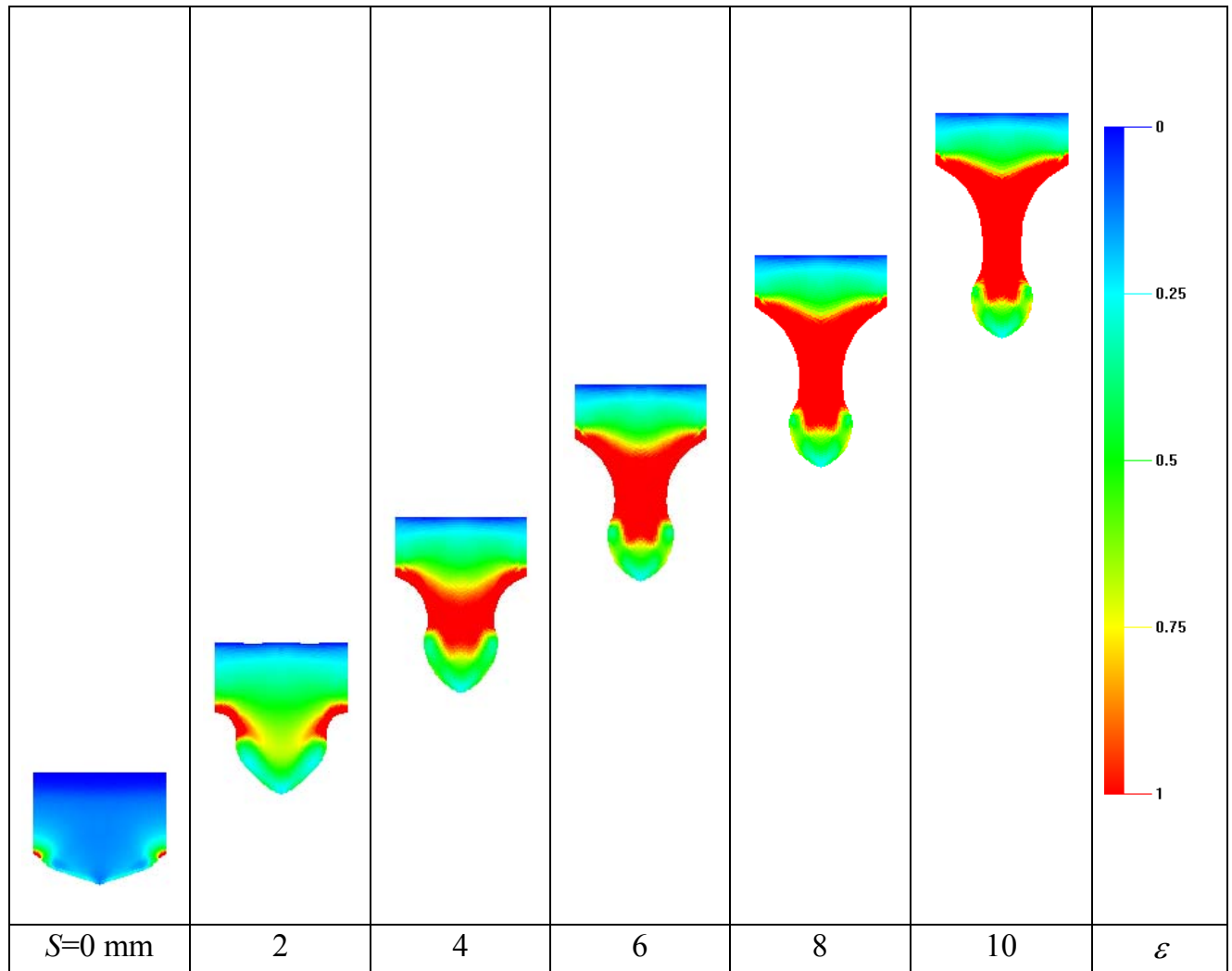| S=0 mm | 2 | 4 | 6 | 8 | 10 | ε |

Table 6.1 presents the scale of analyzed value of plastic strain up to the amplitude equaled to 1 (100 %). In this scale, dynamics of the sample deformation process is shown most informatively at the flight bases up to S=10 mm. At later stages of flight of the liner (S=6÷10 mm), the strain value exceeds significantly the mentioned value of 100 %, and it reaches 200÷300 % in the central part of the sample.

Table 6.2 - Spatial distributions of plastic strain rate in sample versus traveled distance (λ=2 mm, A_0=0.35 mm)
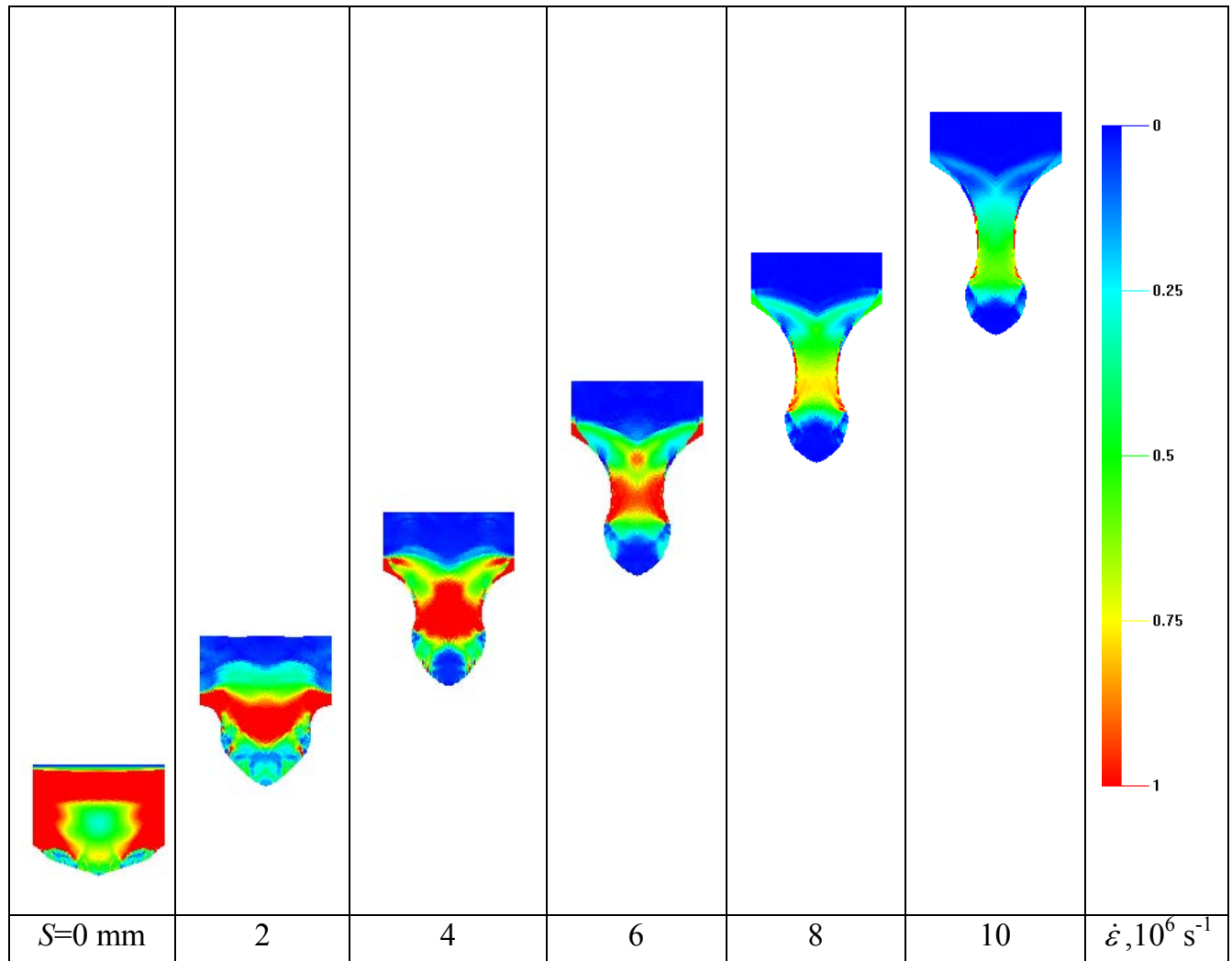

S=0 mm	2	4	6	8	10	$\dot{\varepsilon}$,10^6 s^{-1}

Table 6.3 - Spatial distributions of yield strength in sample versus traveled distance (λ=2 mm, A_0=0.35 mm)

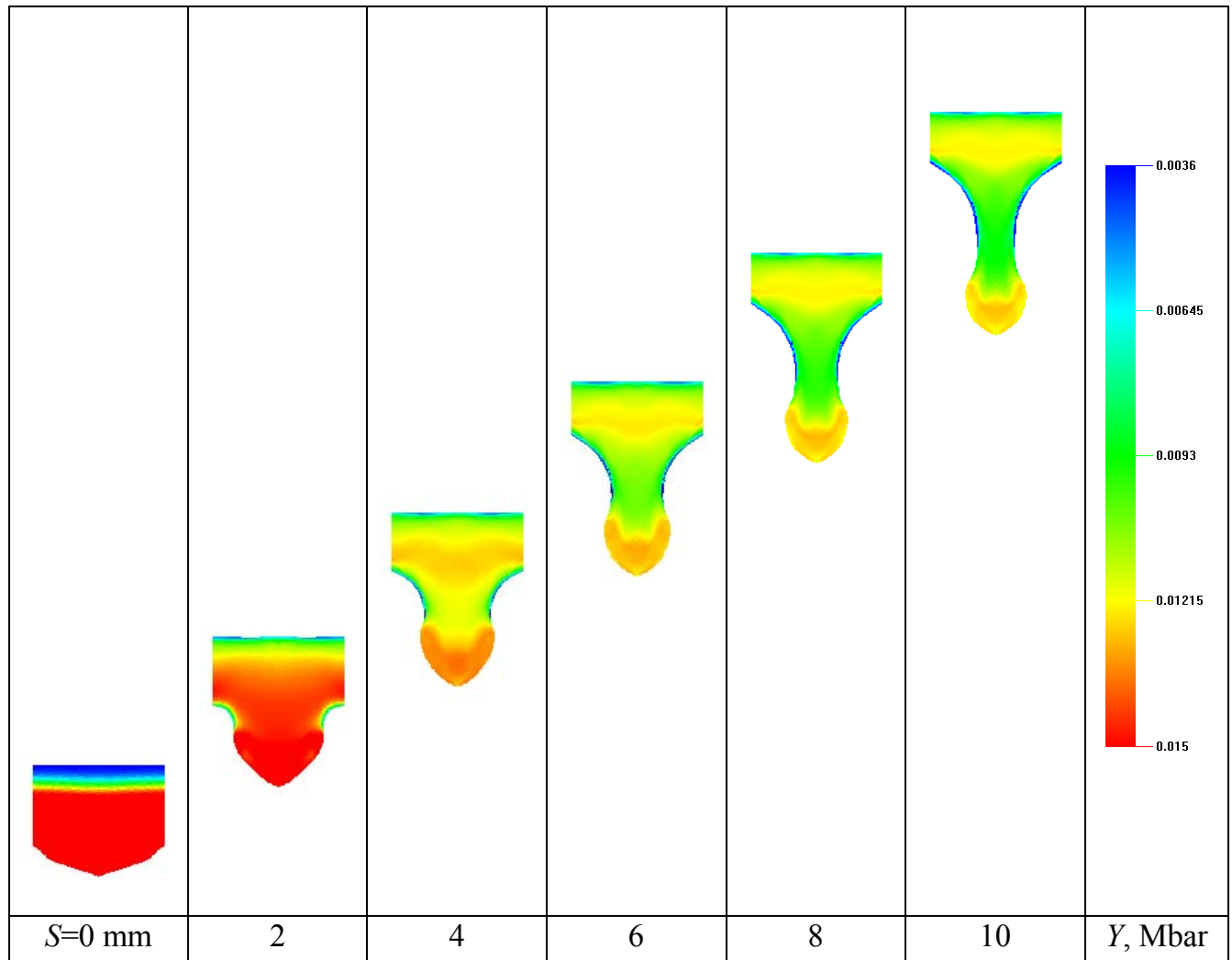
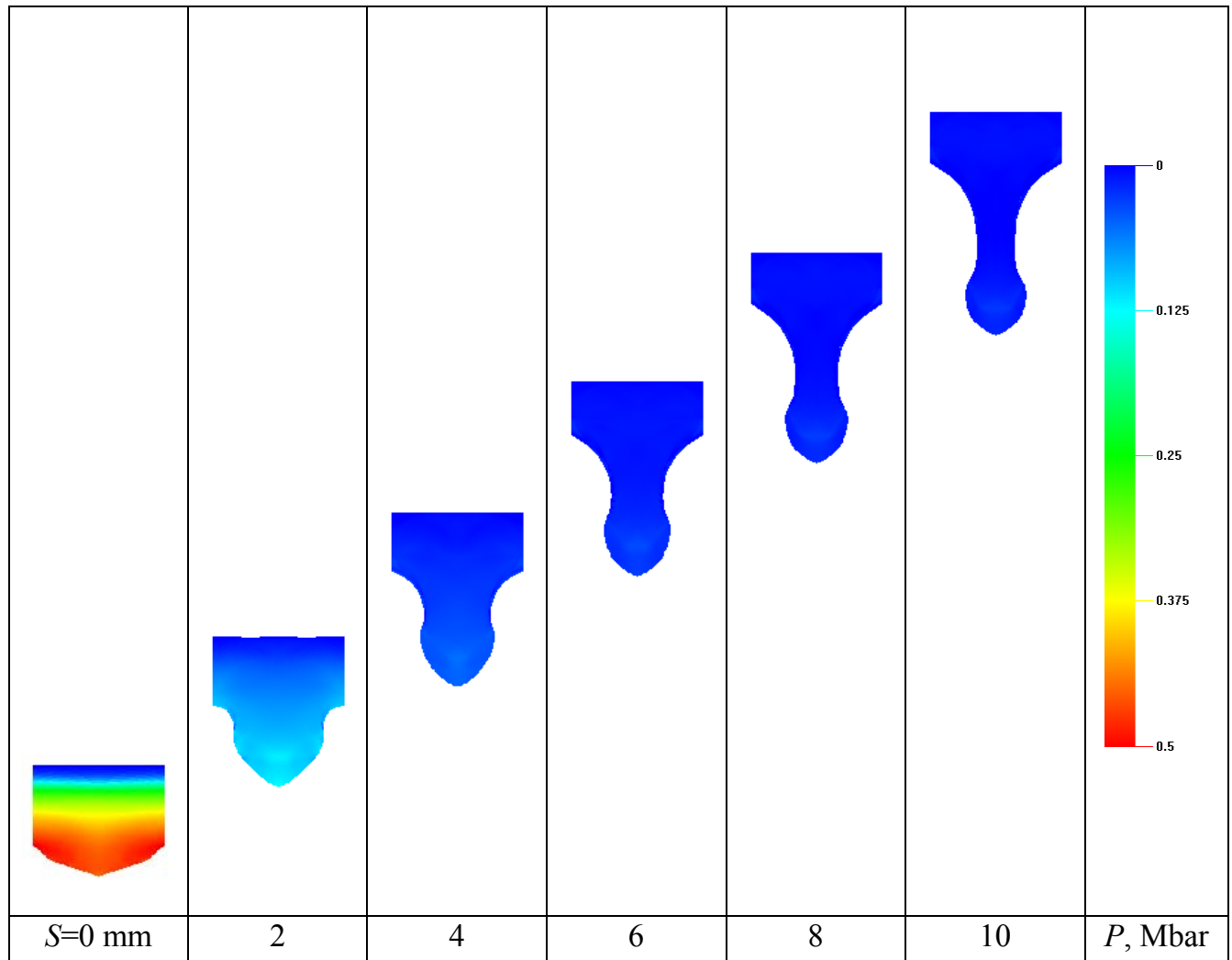| S=0 mm | 2 | 4 | 6 | 8 | 10 | Y, Mbar |

Table 6.4 - Spatial distributions of pressure in sample versus traveled distance (λ=2 mm, A_0=0.35 mm)

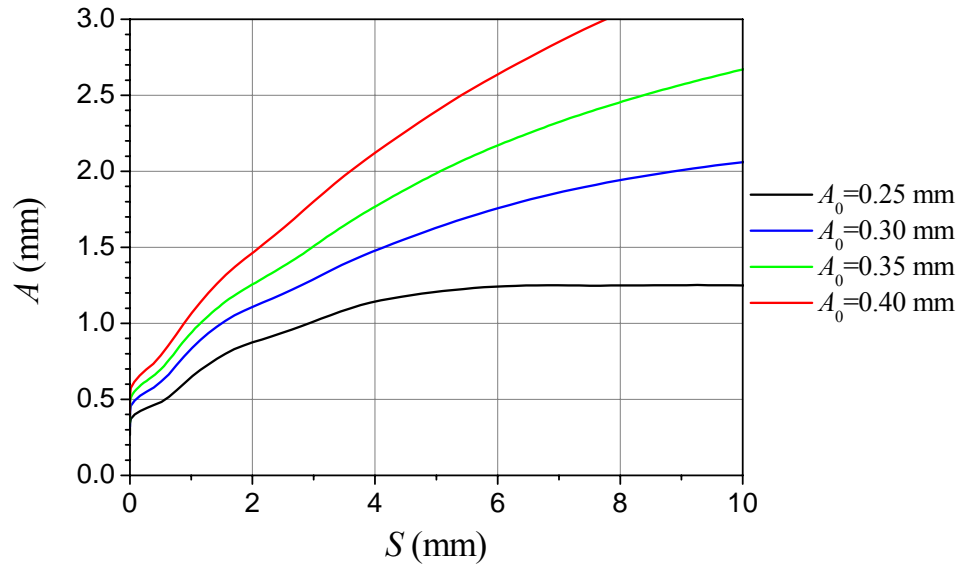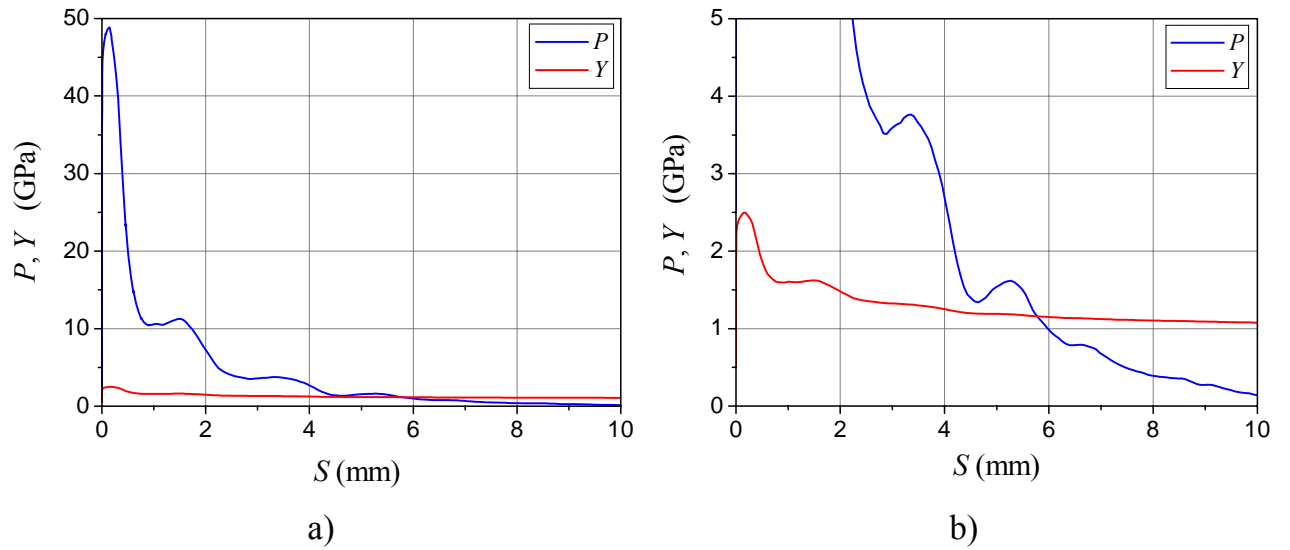| S=0 mm | 2 | 4 | 6 | 8 | 10 | P, Mbar |

Fig. 6.1 – Perturbation amplitude versus time and
distance traveled by liner (S). $P_{max} \approx 50$ GPa, $\lambda = 2$ mm

a) - in middle part of sample where the highest shear strains occur;
b) – increased scale.

Fig. 6.2 – Pressure and dynamic yield strength versus time in middle part of sample

7 Experimental setup for loading Be with recovery of samples

Goal of these investigations is determination how loading influences on *Be* microstructure. Two types of loading can be used in the tests:

- quasi-isentropic compression wave, which is gradually transformed to shock wave (maximum pressure is constant, strain rate is changed from $\dot{\varepsilon}_x \sim 10^5$ to 10^{10} s^{-1});

- loading by a thin metal impactor, which provides several times reduction of amplitude of entering shock wave while it moves in the sample (SW amplitude is changed $P \sim 65 \div 30$ GPa, strain rate is $\dot{\varepsilon}_x \sim 10^{10}$ s^{-1}).

Strain rate can be changed from $\dot{\varepsilon}_x \sim 10^5$ to 10^{10} s^{-1} at various depths of samples. When varying strain rate, the deformation mechanisms are changed. Loss of stability of plastic flow is possible, and transition to heterogeneous regime of deformation is possible at various scale levels. Growth of shear strength in metals due to strain rate (viscosity) increase can be changed for abrupt loss of integral shear strength ($\dot{\varepsilon}_i \geq 10^7$ s^{-1}).

Data of metallographic investigations of *Be* samples, which were recovered after high-rate deformation, will supplement the information, which had been obtained when investigating *Be* at low strain rates (the methods of Hopkinson and Taylor) and by the perturbation method. The data will be used for calibration of the dynamic strength model.

The samples will be investigated by transmission and scanning electron microscope. As a result of the investigations, density of dislocation of twins will be determined.

Series of one-dimensional calculations was performed for selection of possible schemes of quasi-isentropic and shock-wave loadings in the pressure range $P_{\text{load}} \approx 30 \div 60$ GPa with recovery of beryllium samples.

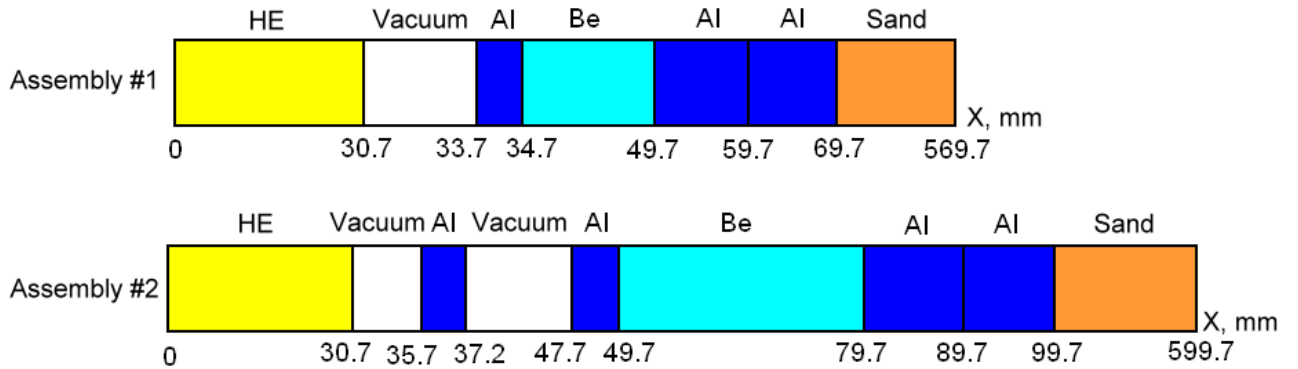Fig. 1.7 presents the one-dimensional schemes of assemblies.

Fig. 7.1 – One-dimensional schemes of axial sections of assemblies with recovery

7.1 Assembly #1. Transition of quasi-isentropic compression wave to shock wave

Fig. 7.2 presents the dependences of stress on time at various depths X of beryllium sample (counting from the loaded surface).
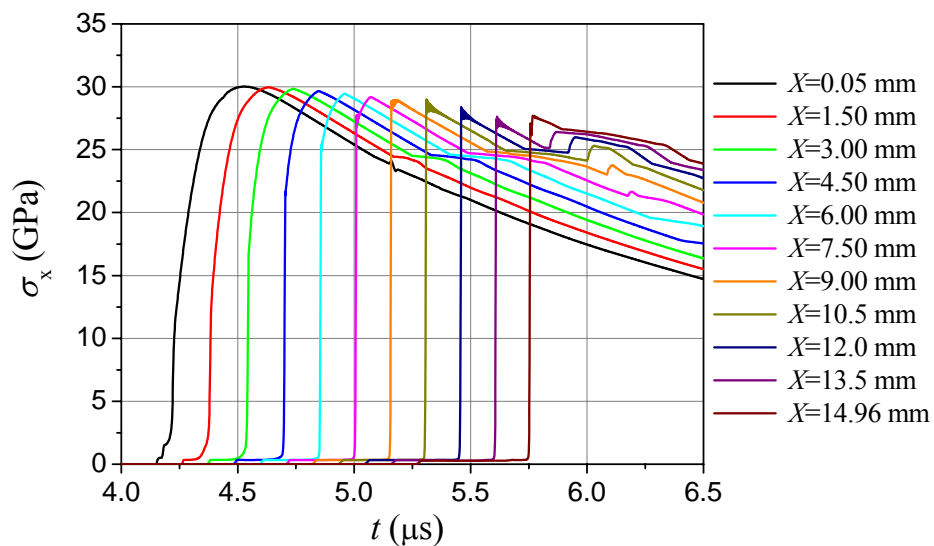

Fig. 7.2 – Stress versus time at various depths X of *Be* sample

Fig. 7.3 presents the dependences of intensity of plastic strain on time at various depths X of beryllium sample (counting from the loaded surface).
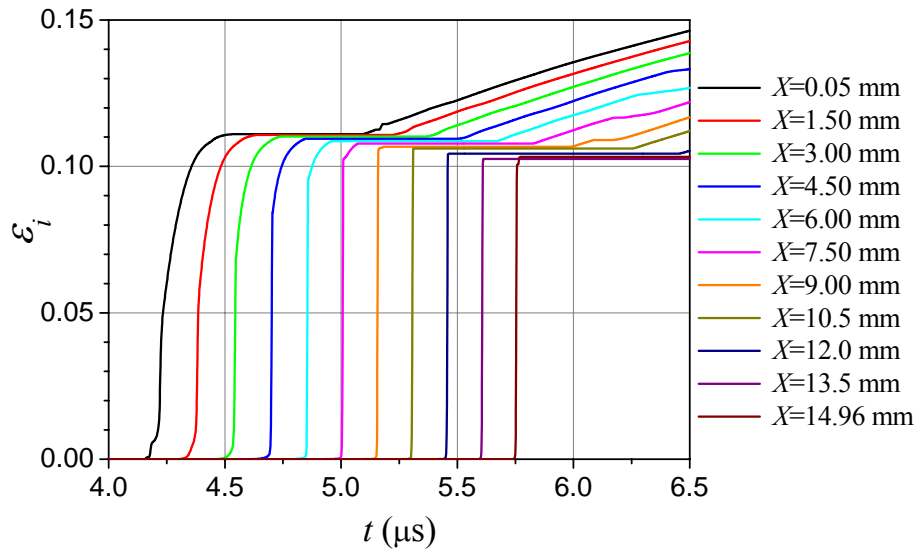
Fig. 7.3 – Intensity of plastic strain versus time at various depths X of beryllium sample

Fig. 7.4 presents the dependences of yield strength on time at various depths X of beryllium sample (counting from the loaded surface).
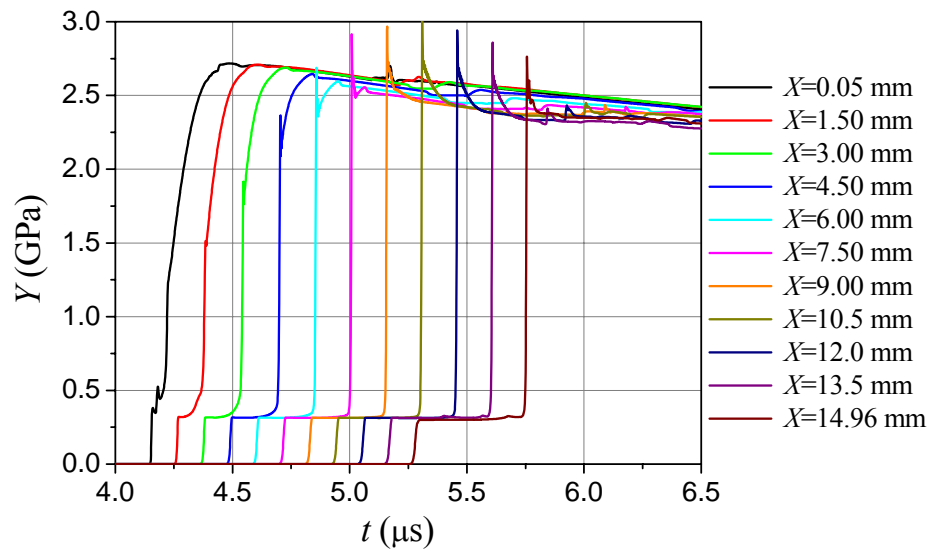

Fig. 7.4 – Yield strength versus time at various depths X of beryllium sample

Fig. 7.5 presents the dependence of temperature on time at various depths X of beryllium sample (counting from the loaded surface). The melting temperature is in the range of 1750÷2300 °K at the same depths of the sample.
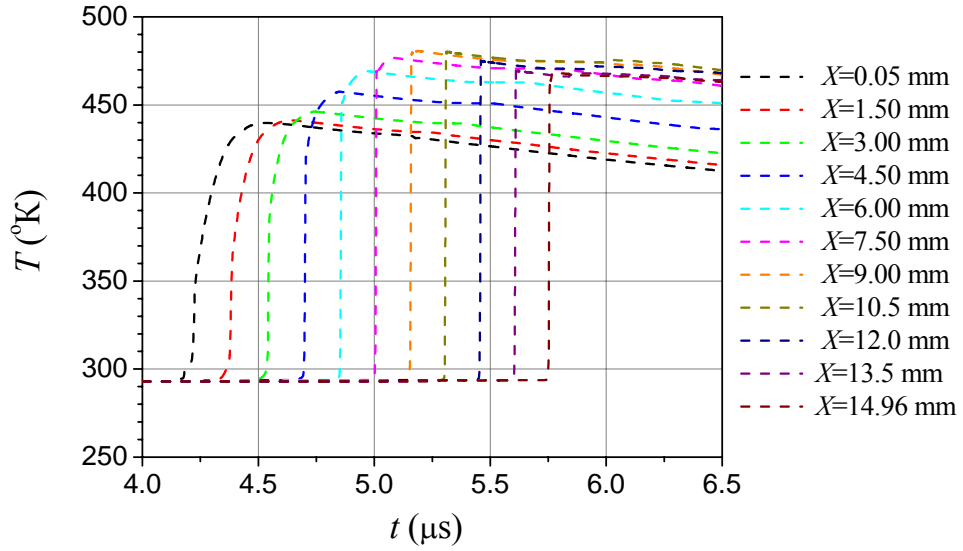
Fig. 7.5 – Temperature versus time at various depths *X* of beryllium sample

7.2 Assembly #2. Loading by shock wave with decreasing amplitude

Fig. 7.6 presents the dependences of stress on time at various depths *X* of beryllium sample (counting from the loaded surface).
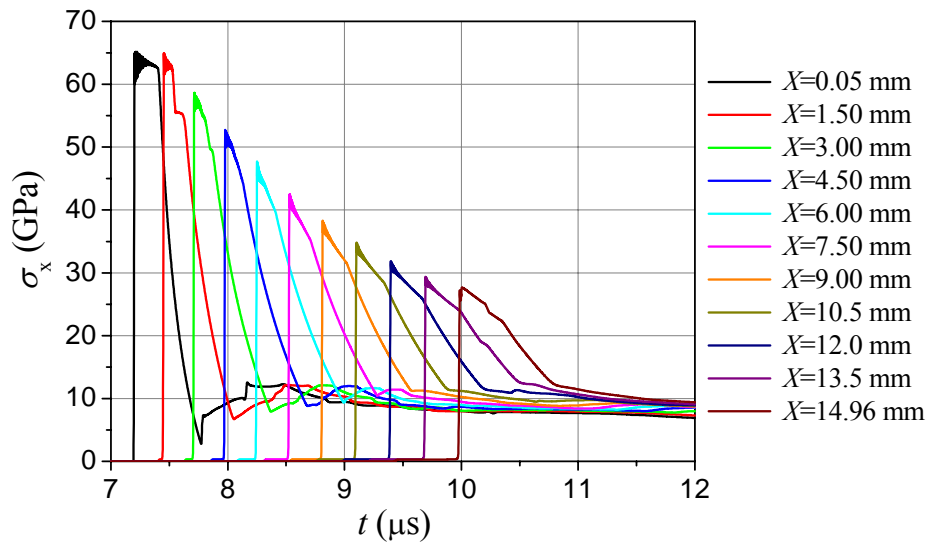

Fig. 7.6 – Stress versus time at various depths *X* of beryllium sample

Fig. 7.7 presents the dependences of intensity of plastic strain on time at various depths *X* of beryllium sample (counting from the loaded surface).
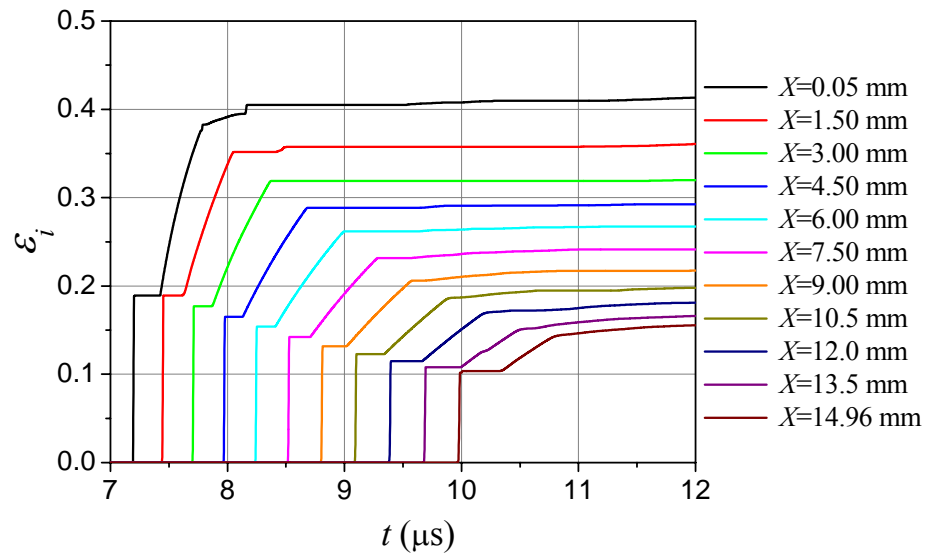

Fig. 7.7 – Intensity of plastic strain versus time at various depths *X* of beryllium sample

Fig. 7.8 presents the dependences of yield strength on time at various depths *X* of beryllium sample (counting from the loaded surface).
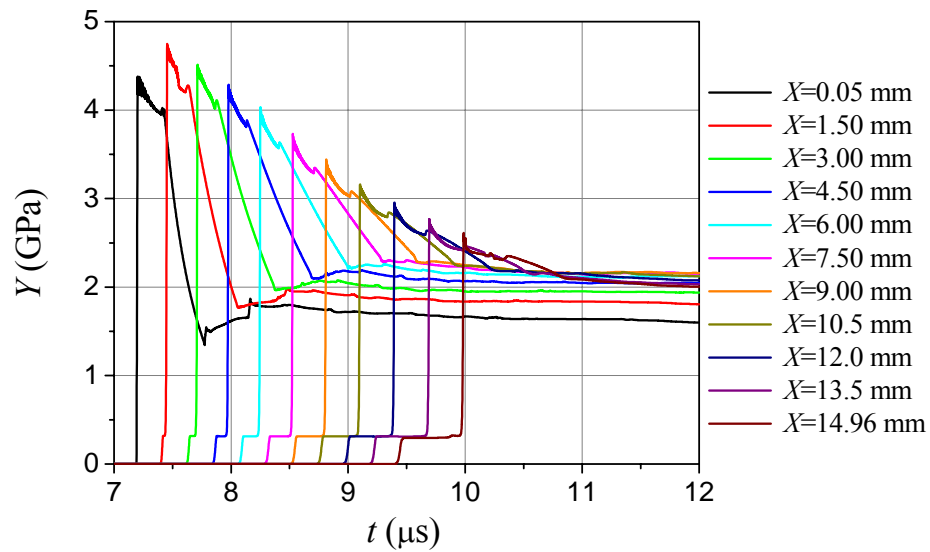

Fig. 7.8 – Yield strength versus time at various depths *X* of beryllium sample

Fig. 7.9 presents the dependence of temperature on time at various depths *X* of beryllium sample (counting from the loaded surface). The melting temperature is in the range of 1750÷2700 °K at the same depths of the sample.

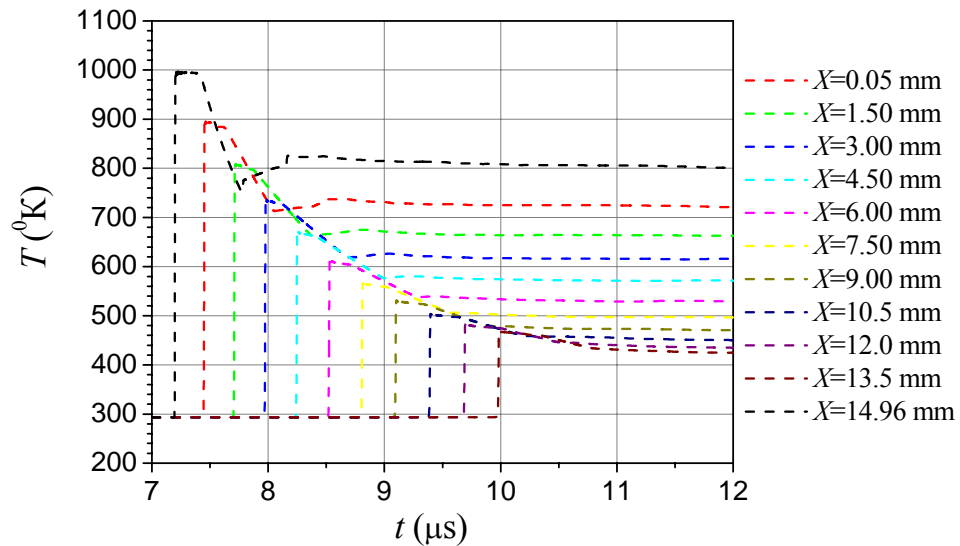Fig. 7.9 – Temperature versus time at various depths *X* of beryllium sample

Conclusion

The report for Task 1 of Agreement # B590737 presents a review of published experimental data on shear strength of *Be*.

Also the known models of beryllium (*S200F*) strength are considered. The relaxation model is chosen for the further investigations. This model has a set of parameters, which provide the most complete description of the available experimental data. The model was published in [21].

Using the relaxation model, numerical justification was performed for the tests aimed to investigate *Be S200F*. The investigation will be accomplished under the frameworks of Task 3 of the Agreement.

The final variant of the experimental setup for the tests will be coordinated with LLNL representative (R. Cavallo).

The report presents results of measurements of vanadium liner velocity by the laser interferometer technique, which was described in report [3].

References

1 A.I. Lebedev, P.N. Nizovtsev, V.A. Rayevsky, V.P. Soloviev.
Rayleigh-Taylor instability in Strong Media. Experimental Study.
5th International workshop on the physics of compressible turbulent mixing. Stony Brook, N.Y., USA, 18-21 July, 1995, p. 231-236.

2 A.I. Lebedev, P.N. Nizovtsev, V.A. Rayevsky, V.P. Soloviev.
Rayleigh-Taylor Instability In Strong Substances: Calculated Experimental Studies of instability in Titanium.
6th International workshop on the physics of compressible turbulent mixing.
Marseille. 1997, p. 307-311.

3 O.N. Aprelkov, V.V. Igonin, A.I. Lebedev, M.O. Lebedeva, V.A. Raevsky, A.M. Podurets et al.
Vanadium dynamic strength measurements.
Report on Task 1 of Agreement # B539457 between LLNL and VNIIEF.
2006, 46 p.

4 O.N. Aprelkov, V.V. Igonin, A.I. Lebedev, M.O. Lebedeva, V.A. Raevsky
Vanadium dynamic strength measurements.
Report on Task 2 of Agreement # B539457 between LLNL and VNIIEF.
2008, 33 p.

5 D. Montoya, G. Naulin, J.P. Ansart.
Comportement dynamique d'une nuance de beryllium.
3 international conference on mechanical and physical behaviour of materials under dynamic loading. Journal de physique IV. 1991, p. 3-27.

6 W.R. Blumenthal, S.P. Abeln, D.D. Cannon, G.T. Gray III, R.W. Carpenter.
Influence of strain rate and temperature on the mechanical behavior of beryllium.
Shock Compression of Condensed Matter, 1997, p. 411-414.

7 Yu.V.Bat'kov, A.P.Bol'shakov, B.L.Glushak, S.A.Novikov, V.A.Sinitsyn.
Strain and strength characteristics of beryllium at high rates of loading (Review). Preprint.
Moscow, TsNIIatominform, 1990, 22 p.

8 M.L. Wilkins, M.W. Guinan.
Impact of cylinders on rigid boundary.
Journ of Appl. Phys, v.44, 1973, p. 1200-1206.

9 Chris D. Adams, William W. Anderson, George T. Gray III, Charles T. Owens, William R. Blumenthal, Franz J. Freibert, Jonny M. Montoya and Paul J. Contreras.
Spall and damage behavior of *S200F* beryllium.
Shock Compression of Condensed Matter – 2009. Edited by M.L.Elert, W.T.Buttler, M.D.Fumish, W.W.Anderson and W.G.Proud. 2009, p. 509-512.

10 V.I. Romanchenko and G.V. Stepanov.
Zh. Prikl. Mekh. Tekh.Fiz., 21, p. 141-147 (1980).

11 Wise J.L., Chhabildas L.C., Asay J.R.
Shock Compression of Beryllium.
Proc. Shock Waves in Condensed Matter. Eds. W.J.Nellis, L.Seaman, R.A.Graham. 1981, p. 417-421.

12 Asay J.R., Chhabildas L.C., Wise J.L.
Strain Rate Effects in Beryllium Under Shock Compression.
Proc. Shock Waves in Condensed Matter. Eds. W.J.Nellis, L.Seaman, R.A.Graham. 1981, p. 427-431.

13 Yu.I. Meshcheryakov, A.K. Divakov, Yu.A. Petrov, C.F. Cline.
On the dynamic plasticity and strength of polycrystalline beryllium.
International Journal of Impact Engineering 30 (2004) 17-29.

14 J.W. Swegle and D.E. Grady.
J. Appl. Phys. 58, 692 (1985).

15 Chhabildas L.C., Wise J.L., Asay J.R.
Reshock and release behavior of beryllium.
Shock Waves in Condensed Metter, 1981, California, p 422-426.

16 C. Deeney.
Dynamic materials experiments on Z in support of Campaigns 2.1 and 2.2.
CEGSNL Working Groups (2006).

17 V.V. Igonin, A.I. Lebedev, M.O. Lebedeva, S.S. Nadezhin, V.A. Raevsky.
Investigations of beryllium dynamic strength**.**
Proceedings of the International Conference XIII Khariton's Topical Scientific Readings
«Extreme states of substance. Detonation. Shock waves».
Sarov, 2011, p. 157-158.

18 Steinberg D., Cochran S., Guiuan M.
A constitutive model for metals applicable at high-strain rait.
Joun. of Appl. Phys. Vol.51. № 3. 1980, p. 1496-1504.

19 Johnson G.R. and Cook W.H.
Proc.7th Intern. Symp. Ballistics, Am. Def. Prep. Org. (ADPA), Netherlands. 1983.

20 Daniel J. Steinberg and Richard W. Sharp.
Interpretation of shock-wave data for beryllium and uranium with an elastic-viscoplastic
constitutive model.
J. Appl. Phys. 52 (8), August 1981, p. 5072-5083.

21 O.N. Ignatova, V.A. Raevsky, S.S. Nadezhin.
Development of constitutive relations of beryllium.
Proceedings of the International Conference XIII Khariton's Topical Scientific Readings
«Extreme states of substance. Detonation. Shock waves».
Sarov, 2011, p. 184-185.

22 M.V. Zhernokletov, V.N. Zubarev, R.F. Trunin, V.E. Fortov.
Experimental data on shock compressibility and adiabatic expansion of condensed
substances at high energy densities.
Chernogolovka, IKhFCh, 1996, 386 p.

23 Physical values.
Reference book under edition of I.S. Grigorieva, E.Z. Meilikhova.
Moscow, Energoatomizdat, 1991.

24 L.V. Al'tshuler, S.E. Brusnikin.
Equation of state of compressed and heated metals.
TVT. # 1. 1987. P.   42-51.

25 L.V. Al'tshuler, S.E. Brusnikin, E.A. Kuzmenkov.
Isotherms and functions of Grueneisen for 25 metals.
PMTF, #1, 1987, p. 134-146.

26 Ph. Legrand and G. Robert.
First-principles thermoelasticity of beryllium.
Shock Compression of Condensed Mater. 2009, p. 513-516.

27 Tom Mehlhorn.
Overview of Sandia High Energy Density Physics Program.
Zababakhin Scientific Talks Snezhinsk.
Chelyabinsk Region, Russia 10-14 September, 2007.

28 S.K. Godunov, B.I. Romensky.
Nonstationary equations of nonlinear theory of elasticity in Eulerian coordinates. PMTF. # 6. 1972, p. 124-144.

29 Dennis E. Grady.
Structed shock waves and the fourth-power law.
Journal of Applied Physics. Vol. 107, 2010, 013506, p. 1-13.

30 C.F. McMillan, D.R. Goosman et al.
Review of Scientific Instruments 59 (1988). № 1, 1-20.

31 V. A. Arinin and B. I. Tkachenko.
Achieving the Ultimate Quality of Image Registration in Radiography.
Pattern Recognition and Image Analysis, 2009, Vol. 19, No. 1, p. 63–68.

32 V. A. Arinin and B. I. Tkachenko.
Use of Abelian transformation for metrological purposes when processing radiographic images.
Proceedings of the International Conference XIII Khariton's Topical Scientific Readings «Extreme states of substance. Detonation. Shock waves».
Sarov, 2011, p. 303-305.

33 V. A. Arinin.
Functional tracing of interface between two media in axially symmetric objects basing on X-ray photos of them.
International Conference «X Zababakhin's Talks», April 15-19, 2010, Snezhinsk, Chelyabinsk reg.

34 N.F. Gavrilov, G.G. Ivanova, V.I. Selin, V.N. Sofronov.
Code UP-OK for solving one-dimensional problems of continuum mechanics in one-dimensional complex.
VANT, 1982, Issue 3(11), p. 11-14.

35 A.I. Abakumov, P.N. Nizovtsev, A.V. Pevnitsky, V.P. Solov'ev.
Program complex DRAKON for calculation of elastic-plastic flows under shock-wave loading in two-dimensional and three-dimensional approximations.
IV Zababakhin's Talks. Proceedings of the International Conference. 1995, p. 227-228.

36 F. Reusch, B. Svendsen, D. Klingbeil.
Local and non-local Gurson-based ductile damage and failure modeling at large deformation.
European Journal of Mechanics A/Solids. 22 (2003), p. 779–792.